ARTICLE

https://doi.org/10.1038/s41586-018-0347-0

Niobium tungsten oxides for high-rate lithium-ion energy storage

Kent J. Griffith[1], Kamila M. Wiaderek[2], Giannantonio Cibin[3], Lauren E. Marbella[1] & Clare P. Grey[1]*

The maximum power output and minimum charging time of a lithium-ion battery depend on both ionic and electronic transport. Ionic diffusion within the electrochemically active particles generally represents a fundamental limitation to the rate at which a battery can be charged and discharged. To compensate for the relatively slow solid-state ionic diffusion and to enable high power and rapid charging, the active particles are frequently reduced to nanometre dimensions, to the detriment of volumetric packing density, cost, stability and sustainability. As an alternative to nanoscaling, here we show that two complex niobium tungsten oxides—$Nb_{16}W_5O_{55}$ and $Nb_{18}W_{16}O_{93}$, which adopt crystallographic shear and bronze-like structures, respectively—can intercalate large quantities of lithium at high rates, even when the sizes of the niobium tungsten oxide particles are of the order of micrometres. Measurements of lithium-ion diffusion coefficients in both structures reveal room-temperature values that are several orders of magnitude higher than those in typical electrode materials such as $Li_4Ti_5O_{12}$ and $LiMn_2O_4$. Multielectron redox, buffered volume expansion, topologically frustrated niobium/tungsten polyhedral arrangements and rapid solid-state lithium transport lead to extremely high volumetric capacities and rate performance. Unconventional materials and mechanisms that enable lithiation of micrometre-sized particles in minutes have implications for high-power applications, fast-charging devices, all-solid-state energy storage systems, electrode design and material discovery.

New high-rate electrode materials that can store large quantities of charge in a few minutes, rather than hours, are required to increase power and decrease charging time in lithium-ion batteries. Such materials can thus help to alleviate technological challenges associated with the adoption of electric vehicles and grid-scale batteries and enable the development of new power-intensive devices. The most intuitive and commonly used approach to increase rate performance is to create nanometre-sized or porous (and often hierarchical) structures, which minimize Li^+ solid-state diffusion distances, enable more rapid Li^+ transport through the composite electrode and increase the surface area of electrode materials in contact with electrolyte. Carbonaceous hierarchical structures and carbon-coating are also frequently used to improve electronic conductivity, which is another prerequisite for the application of high current densities.

In practice, despite excellent lithium mobility, graphite cannot be used at high rates owing to particle fracture and the risk of Li dendrite formation, the latter leading to short circuits and potentially fires and explosions[1–3]. The dendrite issue inherently limits the use of low-voltage anodes in high-rate applications because electrode inhomogeneity, or any source of increased overpotential, can lead to Li plating potentials on the surface of the electrode[3]. $Li_4Ti_5O_{12}$, with an average voltage of 1.55 V (Supplementary Fig. 1), enables high-rate Li (de)intercalation without the risk of Li dendrites or substantial solid–electrolyte interphase formation, albeit with an undesirable but necessary decrease in full-cell voltage and thus energy density. In this well-established 'high'-voltage and high-rate anode, the capacity of 1-μm particles from solid-state synthesis reaches only 60–65 mA h g^{-1} at a rate[4] of 10C, where the C-rate is defined as the inverse of the number of hours required to reach a defined theoretical capacity; for example, 10C corresponds to a 6-min discharge or charge time (see Methods). By contrast, through two decades of research, present carbon-coated nanoparticles of $Li_4Ti_5O_{12}$ can reach at least 150 mA h g^{-1} at 10C[5,6], which corresponds to approximately 0.5 lithium ions per transition metal (Li^+/TM). However, using nanometre-sized and porous materials for electrochemical energy storage applications inherently results in a severe penalty in terms of volumetric energy density. Furthermore, these carefully designed porous and nano-architectures are time consuming and expensive to synthesize, characterize and manufacture. The relevant synthesis methods often result in relatively low yields or the generation of large quantities of chemical waste[7], while also being more susceptible to degradation during electrochemical cycling (from processes such as catalytic decomposition of the electrolyte[8], morphological changes that result in loss of nanostructuring[9] and higher first-cycle capacity loss[10]).

In this work, we break from the conventional strategy of nanoscaling and nanostructuring of electrode materials to overcome poor ionic diffusion and electronic properties (found in TiO_2 and $Li_4Ti_5O_{12}$ for example). We demonstrate that with the appropriate host lattice, none of the usual size, structure or porosity criteria are required to achieve a practical high-rate battery electrode. Instead, we use insight obtained from previous investigations of complex binary niobium oxides, such as the low-temperature polymorph T-Nb_2O_5[11], and of superionic conductors, such as lithium lanthanum titanate perovskite (LLTO)[12], to identify structural motifs that should exhibit favourable Li diffusion properties, and thus superior performance, allowing micrometre-sized particles to be used at extremely high rates. We show that when multi-redox 4*d* and 5*d* transition metals are used with the appropriate three-dimensional oxide structure, we can achieve extremely high volumetric energy densities and impressive rates. The bulk compounds studied are a series of complex 'block' or 'bronze-like' oxide structures (Fig. 1) largely comprising corner- and edge-sharing NbO_6 and WO_6 octahedra, and both oxides are prepared via gram-scale solid-state synthesis. Their unusual electrochemical performance is first illustrated by studying large (3–10 μm primary, 10–30 μm agglomerate) dense

[1]Department of Chemistry, University of Cambridge, Cambridge, UK. [2]X-ray Science Division, Advanced Photon Source, Argonne National Laboratory, Argonne, IL, USA. [3]Diamond Light Source, Harwell Science and Innovation Campus, Didcot, UK. *e-mail: cpg27@cam.ac.uk

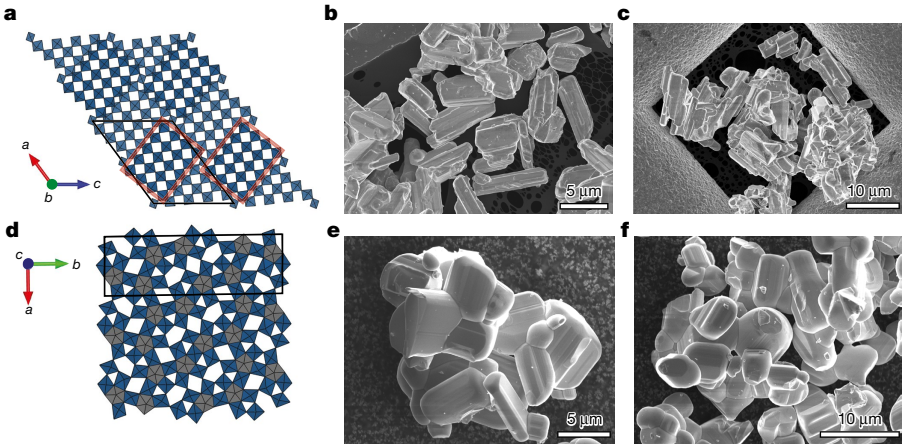

Fig. 1 | Crystal structure and particle morphology of $Nb_{16}W_5O_{55}$ and $Nb_{18}W_{16}O_{93}$. a–c, $Nb_{16}W_5O_{55}$ is built from blocks (red rectangles) of 4 × 5 (Nb,W)O_6 octahedra, with adjoining blocks forming crystallographic shear planes. (Nb,W)O_4 tetrahedra connect the corners of the blocks. **a**, A view down the *b* direction of the structure. **b**, **c** Electron images of the micrometre-sized particles. **d–f**, $Nb_{18}W_{16}O_{93}$ is a superstructure of the tetragonal tungsten bronze (blue) with pentagonal tunnels (grey) partially filled by –W–O– chains that form pentagonal bipyramids. **d**, A view down the *c* direction, depicting the various tunnels. **e**, **f**, Electron images. In **a** and **d**, the black boxes indicate the unit cells.

particles of the block structure $Nb_{16}W_5O_{55}$ (Fig. 1a–c). Even on a mass-normalized basis, the lithium storage performance of $Nb_{16}W_5O_{55}$ exceeds that of nanostructured versions of the heavily studied $Li_4Ti_5O_{12}$[5,13–15], TiO_2(B)[16–18] and T-Nb_2O_5[19–21] under similar loading conditions. Given the high density of the crystal structure and the high tap density of bulk $Nb_{16}W_5O_{55}$ compared with nanomaterials, this leads to exceptionally high volumetric performance. We further demonstrate the generality of this bulk phenomenon by exploring another new electrode material, bronze-like $Nb_{18}W_{16}O_{93}$ (Fig. 1d–f).

Complex oxides for energy storage

$Nb_{16}W_5O_{55}$ is a metastable member of the system Nb_2O_5–WO_3[22], with a monoclinic structure composed of subunits of corner-shared octahedra arranged into ReO_3-like blocks that are four octahedra wide by five octahedra long and infinite in the third dimension (Fig. 1a)[23]. The block subunits are connected by crystallographic shear planes along the edges and by tetrahedra at each corner, and the structure is expressed as $(4 \times 5)_1$; in the notation $(m \times n)_p$, *m* and *n* denote block length in units of octahedra and *p* relates to the connectivity of the blocks, which may also be joined in pairs ($p = 2$) or infinite ribbons ($p = \infty$). To the best of our knowledge, this is the first reported application of any kind for $Nb_{16}W_5O_{55}$ since its discovery in 1965[23,24]. $Nb_{18}W_{16}O_{93}$ is orthorhombic, a $1 \times 3 \times 1$ superstructure of the classic tetragonal tungsten bronze (Fig. 1d, Supplementary Fig. 2). The superstructure[25] results from partial filling of pentagonal tunnels by –M–O– chains to form pentagonal bipyramids, in addition to the distorted octahedra of the tetragonal tungsten bronzes. $Nb_{16}W_5O_{55}$ and $Nb_{18}W_{16}O_{93}$ were prepared via co-thermal oxidation of pellets of NbO_2 and WO_2. Details and alternative synthetic routes are described in Methods (Supplementary Figs. 3–7).

Reaction of $Nb_{16}W_5O_{55}$ with lithium (Fig. 2a) proceeds in three regions from 2.5 V to 1.0 V, with an average voltage of 1.57 V (Supplementary Fig. 1), comparable to the average voltage[26] of 1.55 V of $Li_4Ti_5O_{12}$. The three regions, more easily observed in the derivative plot (Fig. 2b), are characterized by their slope and are reminiscent of the three regions observed in other crystallographic shear structures[27], such as a second niobium oxide polymorph, H-Nb_2O_5[28], PNb_9O_{25}[29], $TiNb_2O_7$[30] and $Nb_{12}WO_{33}$[31]. When the kinetics were examined over a range of current densities from C/5 (34.3 mA g^{-1}) to 60C (10.3 A g^{-1}), $Nb_{16}W_5O_{55}$ showed unprecedented bulk rate performance (Fig. 2a, b, e) in standard electrode formulations (see Methods and Supplementary Fig. 8). At C/5, around 1.3 Li^+/TM can be reversibly intercalated for a gravimetric capacity of about 225 mA h g^{-1}. When the rate is increased by a factor of 25 to 5C, $Nb_{16}W_5O_{55}$ maintains a capacity of 1.0 Li^+/TM (171 mA h g^{-1}). At 20C, which corresponds to a three-minute discharge, it is still possible to exchange 0.86 Li^+/TM and access 148 mA h g^{-1}. Rate tests on $Nb_{16}W_5O_{55}$ were performed with a potentiostatic hold at the top of charge to ensure a reliable starting point for discharge. To test the performance under more demanding conditions, 1,000 cycles were measured with fixed galvanostatic discharge and charge conditions of 10C for 250 cycles followed by 20C for 750 cycles with no voltage hold (Fig. 2f). Under these conditions, 0.90 Li^+/TM (average 155 mA h g^{-1}) were reversibly intercalated at 10C with 95% capacity retention after 250 cycles on non-optimized or calendared electrodes. At 20C, the capacity was 0.75 Li^+/TM (average 128 mA h g^{-1}) and the capacity retention was again 95% over 750 cycles at 20C.

Excellent electrochemical energy storage was also discovered in another niobium tungsten oxide with distinct structural motifs: micrometre-scale particles of the bronze-like phase $Nb_{18}W_{16}O_{93}$ (Fig. 1d–f) showed enhanced rate performance and could be cycled at extremely high rates (Fig. 2c–f). The average voltage of $Nb_{18}W_{16}O_{93}$ is 1.67 V (Supplementary Fig. 1). In terms of gravimetric capacity, $Nb_{18}W_{16}O_{93}$ stores about 20 mA h g^{-1} less than $Nb_{16}W_5O_{55}$ at C/5 and 1C owing to the higher molar mass of the tungsten-rich bronze phase. However, at 20C, $Nb_{18}W_{16}O_{93}$ is still able to accommodate a full unit of Li^+/TM for a capacity of approximately 150 mA h g^{-1}. At 60C and 100C (14.9 A g^{-1}), the capacity is 105 and 70 mA h g^{-1}, respectively.

Other cycling conditions, such as long-term cycling at C/5, and the effect of current collectors, which cannot be ignored at high rates[32], were examined (Supplementary Fig. 9, 10). As a control, Li||Li symmetric cells were cycled at current densities corresponding to those applied for C/5–100C in Fig. 2 (Extended Data Fig. 1a). The overpotentials in the symmetric cell closely match those observed in the electrochemical cycling curves of Fig. 2a–d. This suggests that the extremely high rates in a bulk electrode approach the limits of Li metal plating/stripping or lithium-ion desolvation and transport in carbonate ester electrolytes at room temperature; that is, a considerable fraction of the ohmic loss during fast charging results from the Li metal and electrolyte rather than the complex oxide electrode materials.

Measuring diffusion coefficients in mixed ionic–electronic conductors

The extremely high mobility of Li^+ ions in these systems enabled the direct measurement of lithium diffusion with the pulsed-field-gradient nuclear magnetic resonance (PFG NMR) spectroscopy technique, which has previously only been applied to liquids or diamagnetic superionic solid electrolytes (Extended Data Table 1). To handle the short T_2 (spin–spin) relaxation times of ^{7}Li nuclei, which generally prevent these measurements in electrode materials because they are mixed ionic–electronic conductors, experiments were performed in the

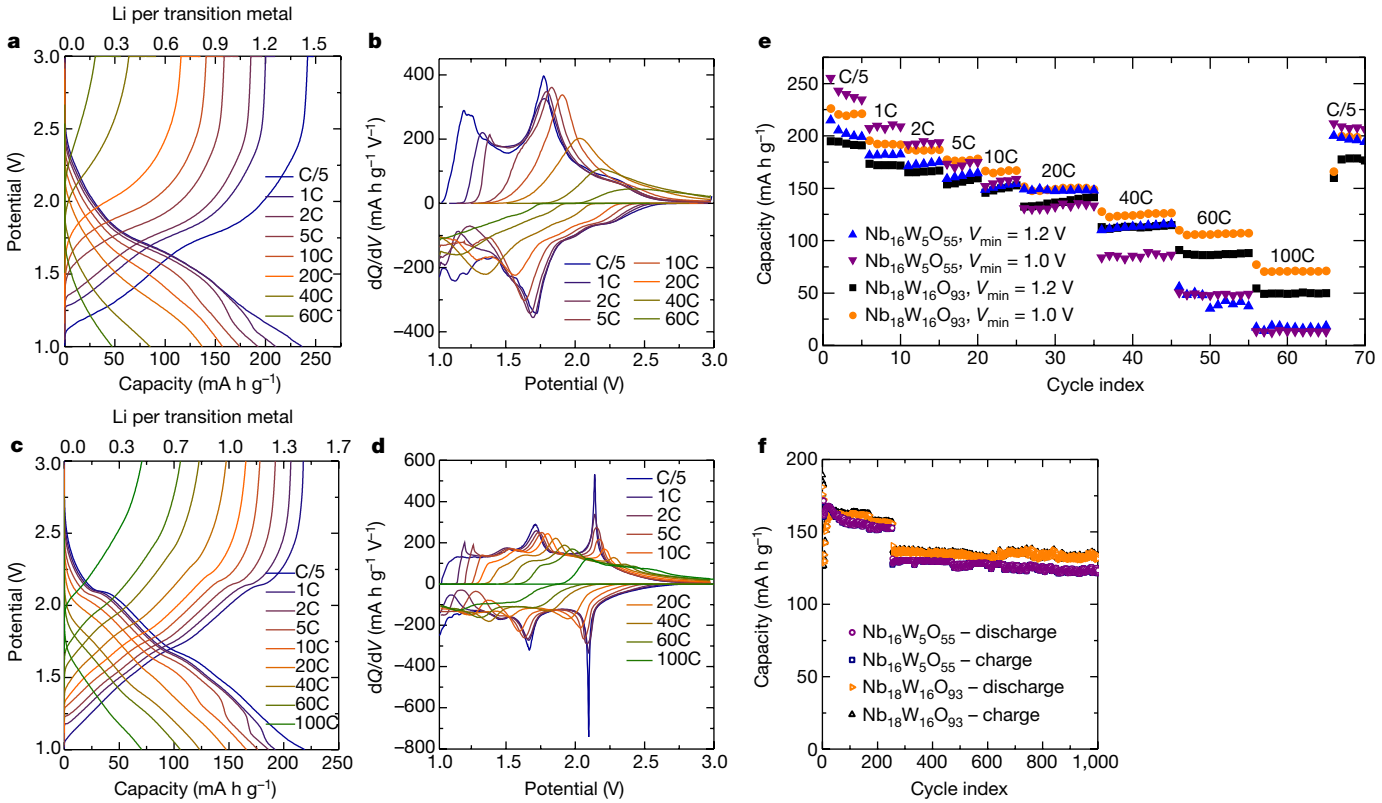

Fig. 2 | Electrochemistry of $Nb_{16}W_5O_{55}$ and $Nb_{18}W_{16}O_{93}$. **a**–**d**, Galvanostatic discharge and charge curves and dQ/dV plots (Q, capacity; V, voltage) of bulk $Nb_{16}W_5O_{55}$ (**a**, **b**) and $Nb_{18}W_{16}O_{93}$ (**c**, **d**) from C/5 up to 100C. **e**, Rate performance summary based on gravimetric capacity. **f**, High-rate cycling for 250 cycles at 10C, followed by 750 cycles at 20C. Dense electrodes of large particles with active mass loading of 2–3 mg cm^{-2} were tested at current densities corresponding to discharge times of several hours to tens of seconds. $Nb_{16}W_5O_{55}$ was charged with a 1-h constant-voltage step at the top of charge to ensure a comparable starting point on discharge; $Nb_{18}W_{16}O_{93}$ was cycled without this hold step for all measurements and stored over 100 mA h g^{-1} at 60C (that is, in less than 60 s). High-rate cycling for 1,000 cycles was performed on both oxides at 10C and 20C and at a constant current, without a potentiostatic step.

temperature range 333–453 K, at which the T_2 relaxation times were longer than at room temperature. Analysis of the data (Extended Data Fig. 2, Methods) for $Li_xNb_{16}W_5O_{55}$ ($x = 6.3$, 8.4) and $Li_xNb_{18}W_{16}O_{93}$ ($x = 3.4$, 6.8, 10.2) showed lithium transport above 10^{-13} m^2 s^{-1} at 333 K and 10^{-12} m^2 s^{-1} at 373 K. Assuming Arrhenius behaviour and the extremely low measured activation energies of 0.10–0.30 eV, the room-temperature lithium diffusion coefficients are estimated to be greater than 1×10^{-13} m^2 s^{-1} for all the materials (Table 1). The different samples exhibited similar diffusion coefficients and activation energies, consistent with the transport measurements made with the galvanostatic intermittent titration technique (GITT) (see Methods and Extended Data Fig. 1b, c) at low-to-moderate lithium contents. Lithium diffusion in both niobium tungsten oxide structures is markedly faster than that of $Li_{4+x}Ti_5O_{12}$ or Li_xTiO_2 (about 10^{-16}–10^{-15} m^2 s^{-1}) and is close to that of the best known lithium solid electrolytes (Extended Data Table 1). GITT and ^{7}Li PFG NMR spectroscopy results (Extended Data Figs. 1b and 2, respectively) indicate that this rapid motion is maintained to high lithium contents (≥1.5 Li$^+$/TM), and then the diffusion drops by about two orders of magnitude towards 2.0 Li$^+$/TM. These complementary techniques suggest that the inherent range of the niobium tungsten oxide electrode materials for high-rate multi-redox extends to approximately 1.5 Li$^+$/TM. The diffusion coefficients, of the order of 10^{-12}–10^{-13} m^2 s^{-1}, measured for these materials are consistent with the values required to achieve full lithiation of 10-μm particles on a 60C timescale (Supplementary Table 1).

Table 1 | Lithium diffusion coefficients, obtained from PFG NMR

Component	D_{Li} (m^2 s^{-1}) at 298 K	D_{Li} (m^2 s^{-1}) at 413 K	E_a (eV)
$Li_{6.3}Nb_{16}W_5O_{55}$-a (15%)	2.1×10^{-12}	2.7×10^{-11}	0.23 ± 0.04
$Li_{6.3}Nb_{16}W_5O_{55}$-b (85%)	1.7×10^{-13}	5.2×10^{-13}	0.10 ± 0.04
$Li_{8.4}Nb_{16}W_5O_{55}$	1.6×10^{-13}	6.5×10^{-13} (403 K)	0.13 ± 0.01
$Li_{3.4}Nb_{18}W_{16}O_{93}$	1.1×10^{-13}	2.0×10^{-12}	0.27 ± 0.03
$Li_{6.8}Nb_{18}W_{16}O_{93}$	1.1×10^{-13}	1.8×10^{-12}	0.30 ± 0.01
$Li_{10.2}Nb_{18}W_{16}O_{93}$	1.1×10^{-13}	2.7×10^{-12}	0.29 ± 0.01

The lithium diffusion coefficients, D_{Li}, were measured directly at 333–453 K and extrapolated from the activation energy, E_a, to room temperature, where the relaxation time T_2 was too short to allow direct measurement. Error estimates for activation energies are derived from the standard error of the linear fit. Error bars for the diffusion coefficients are given in Extended Data Fig. 2. The two diffusion components observed in $Li_{6.3}Nb_{16}W_5O_{55}$ are denoted as '-a' and '-b' with 15% and 85% signal contribution, respectively.

Redox activity and local atomic structure

To understand (i) the nature of the charge-transfer sequence as a function of lithiation and (ii) the origin of multielectron redox behaviour in $Nb_{16}W_5O_{55}$ and $Nb_{18}W_{16}O_{93}$, the X-ray absorption near-edge structure (XANES) of the Nb K edge and W L edges was analysed (Supplementary Fig. 11, Methods). For $Nb_{16}W_5O_{55}$, operando and ex situ Nb K edge XANES spectra show a nearly linear trend between the number of electrons (and Li$^+$) transferred and the oxidation state of niobium, extracted from the shift of the absorption edge (Fig. 3a, Extended Data Fig. 3, Supplementary Fig. 12). Similarly, ex situ samples measured at the W $L_{II,I}$ edges show a steadily negative correlation between capacity and edge position; however, there appears to be a larger shift in the tungsten absorption edge for the first 0.5 Li$^+$/TM inserted (Fig. 3b, Extended Data Fig. 3, Supplementary Fig. 12), indicating a slight preference for tungsten reduction initially. The situation for $Nb_{18}W_{16}O_{93}$ (Fig. 3, Extended Data Fig. 4, Supplementary Fig. 12) is analogous in that the niobium oxidation state decreases nearly linearly and tungsten reduction is slightly favoured initially. However, there is a

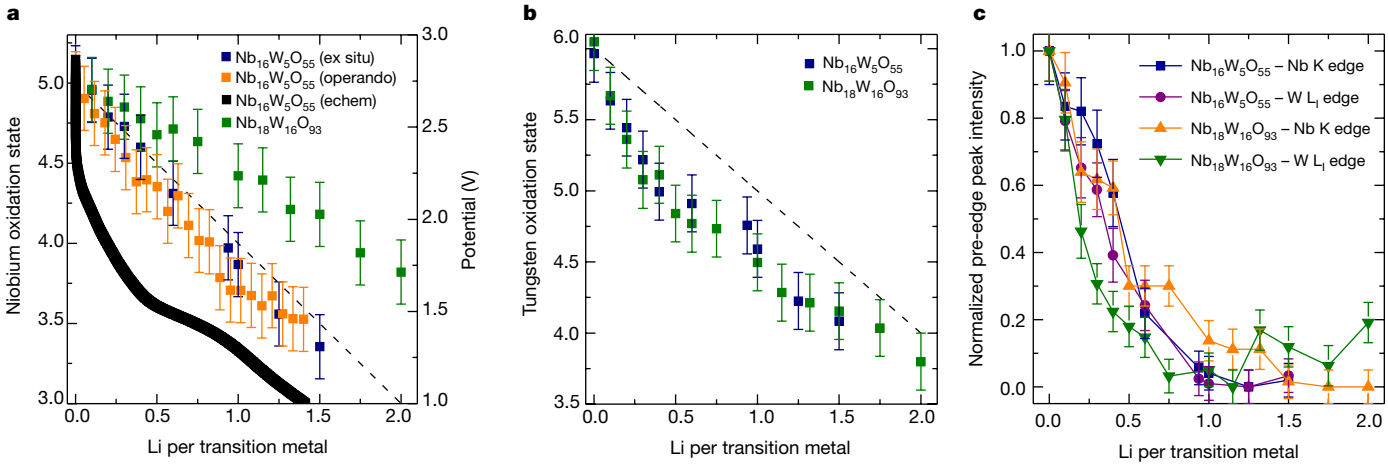

Fig. 3 | X-ray absorption spectroscopy of $Nb_{16}W_5O_{55}$ and $Nb_{18}W_{16}O_{93}$. **a**, **b**, Oxidation states of niobium (**a**) and tungsten (**b**) as a function of lithiation, extracted from shifts in the absorption energy of the Nb K edge and the W L_{II} edge. The black dashed line demarcates a slope of −1, for reference. Oxidation-state error bars are estimated to be ±0.2 on the basis of energy data resolution. The operando electrochemical discharge profile ('echem') is included in **a**. **c**, Pre-edge integrated peak intensity from the Nb K edge and W L_I edge serves as a measure of local distortion from SOJT effects on d^0 octahedral sites and, as the SOJT effect is relaxed upon reduction to d^1 (see Methods for further discussion), a further indication of the oxidation state. Pre-edge integrated peak intensity error bars represent 2σ from Levenberg–Marquardt nonlinear least-squares minimization fits (see Methods and Supplementary Fig. 13).

clear preference for multielectron reduction on the tungsten throughout the lithiation, with Nb^{3+} appearing only beyond 1.5 Li^+/TM, which may be related to cation occupancy variation on octahedral versus pentagonal bipyramidal sites.

The redox centres Nb^{5+} and W^{6+} in $Nb_{16}W_5O_{55}$ are both d^0 and both of these cations located in six-coordinate environments experience second-order Jahn–Teller (SOJT) distortions, which give rise to a pre-edge feature before the main absorption edge in the Nb K and W L_I edge X-ray absorption spectra (Extended Data Figs. 3, 4, Supplementary Figs. 13, 14, Methods); this serves as a direct probe of local symmetry and an additional measure of the oxidation state. As the d^0 cations are reduced, the energy of the d states moves up and the SOJT distortion is reduced (Methods), which increases the local octahedral symmetry and decreases the pre-edge states and intensity monotonically (Fig. 3c, Extended Data Figs. 3, 4, Supplementary Fig. 13)[23], again with a slightly larger effect on tungsten at low lithium concentrations and a bigger difference between tungsten and niobium in $Nb_{18}W_{16}O_{93}$. By about 0.8–1.0 Li^+/TM, both the Nb K and W L_I distinct pre-edges of both the block and bronze phase have decreased and no substantial further changes are observed in compositions corresponding to multi-redox; thus, lithiation is associated with an increase in local symmetry for the d^0 oxide intercalation hosts. The XANES edge shifts and pre-edge evolution for $Nb_{16}W_5O_{55}$ and $Nb_{18}W_{16}O_{93}$ observed in this work indicate a parallel reduction pathway and multielectron charge storage of both transition metals.

Anisotropic host–lattice response to Li intercalation

To probe the lattice evolution of these complex oxides upon lithiation, operando synchrotron X-ray diffraction was performed at different cycling rates. At C/2, $Nb_{16}W_5O_{55}$ evolves through a complex, three-stage solid-solution mechanism (Fig. 4a, c, Extended Data Figs. 5, 6) that correlates with the following observed electrochemical regions: (i) high voltage (until about 65 mA h g^{-1} or 0.4 Li^+/TM): a–c-plane expansion of the blocks, along with a slight expansion perpendicular to the block plane; (ii) about 65–170 mA h g^{-1} (0.4–1.0 Li^+/TM): anisotropic behaviour involving a contraction of the blocks and a substantial expansion in the (perpendicular) b direction; (iii) multi-redox (beyond 1.0 Li^+/TM): linear expansion in all dimensions. The volume expansion is considerably buffered by the block contraction in the second stage, and the lattice undergoes only 5.5% expansion at lithiation to 1.0 Li^+/TM. The diffraction results show that although the second electrochemical process has a relatively small gradient it is not two-phase, in agreement with the GITT measurements (Extended Data Fig. 1b, c). Upon charging, the stages are reversed (Extended Data Fig. 6k, l), although there is some first-cycle capacity loss. This capacity loss is ascribed, at least in part, to residual Li in the structure (Extended Data Fig. 7), rather than the usual solid–electrolyte interphase formation, because the final lithium ions are considerably harder to extract as their removal would lead to the formation of insulating domains. At a ten-times-higher rate (5C), only the first two stages of lattice evolution are observed (Extended Data Figs. 5, 6), which is consistent with the degree of loss of capacity at higher rates. In addition, there is more strain and reaction inhomogeneity at 5C, consistent with previous in situ studies that clearly showed that at these rates, lithium transport within the electrolyte results in internal (electrolyte) inhomogeneities and concentration gradients[33,34]. Nevertheless, the mechanism remains solid-solution in nature, which is evident from the high inter-peak intensity (Extended Data Fig. 6j).

Operando diffraction measurements of $Nb_{18}W_{16}O_{93}$ were performed at rates of up to 10C (Fig. 4b, d; Extended Data Figs. 5, 8, Supplementary Fig. 15). Like the block phase, the bronze phase shows a complicated but reversible nonlinear and strongly anisotropic structural evolution upon lithiation (Fig. 4b, d; see Methods for further discussion). Interestingly, the $b \approx 3a$ pseudo-superstructure relationship persists until the fourth intercalation region, at >0.5 Li^+/TM. From this point, the unit-cell volume actually decreases with increasing lithium intercalation and is the same at 1.0 Li^+/TM as at 0.5 Li^+/TM—a total increase of only 2.8% from the unlithiated host. This volume contraction upon lithium insertion is phenomenologically related to negative thermal expansion[35,36] or negative linear compressibility[37] and may have shared origins related to tilting of the polyhedral units (see 'Host features and design considerations'). The small volume change has implications for the suppression of intergranular cracking and long-term cycle performance[38]. Unlike in the shear structure, the bronze phase exhibits a compositionally narrow two-phase reaction between approximately $Li_{6.6}Nb_{18}W_{16}O_{93}$ and $Li_{10.2}Nb_{18}W_{16}O_{93}$ (0.2–0.3 Li^+/TM); the phase transition preserves the *Pbam* space-group symmetry and is characterized by a–b-plane expansion and contraction of the bronze layers. The structural stability of both the block and bronze phases is also reflected in the stability of the energy storage capacity over 1,000 discharge–charge cycles (Fig. 2f).

Host features and design considerations

Relative to the parent ReO_3 structure, the niobium tungsten oxides accommodate anion-deficient nonstoichiometry by forming topologically distinct condensed phases. This has important consequences for Li motion because the intersecting crystallographic shear planes

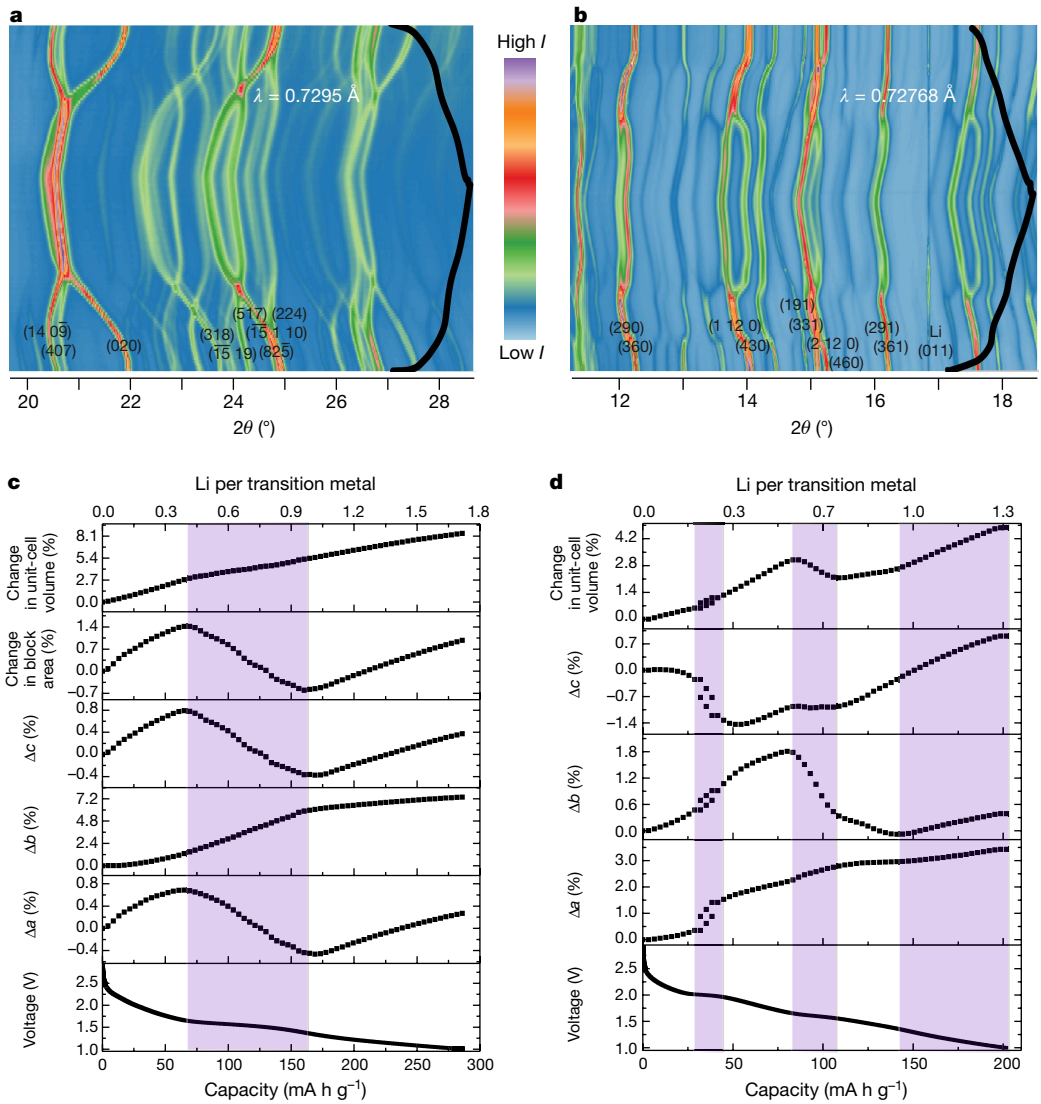

Fig. 4 | Nonlinear structural evolution of $Nb_{16}W_5O_{55}$ and $Nb_{18}W_{16}O_{93}$ from operando synchrotron diffraction. a, **b**, Operando diffraction pattern sections of $Nb_{16}W_5O_{55}$ (**a**) and $Nb_{18}W_{16}O_{93}$ (**b**), with some of the strongest reflections labelled and the electrochemistry overlaid. θ, diffraction angle; I, intensity. **c**, Upon lithiation, block-phase $Nb_{16}W_5O_{55}$ evolves in three stages in the range 3.0–1.0 V at C/2; the expansion is buffered by block contraction in the second stage. **d**, Bronze-like-phase $Nb_{18}W_{16}O_{93}$ evolves through six stages upon lithiation in the range 3.0–1.0 V at 1C. In this complex oxide, volume expansion is buffered by layer contraction in the second stage (two-phase) and b-axis contraction in the fourth and fifth stages. Alternating white and purple shading serves as a guide to the eye to demarcate reaction stages.

(block phase) or twisted octahedra locked to pentagonal columns (bronze-like) (Fig. 1a, d) decrease the structural degrees of freedom. Both the block ($Nb_{16}W_5O_{55}$) and bronze ($Nb_{18}W_{16}O_{93}$) structural motifs are derived from the parent ReO_3 structure type, of which WO_3 is a locally distorted analogue and LLTO is a version with Li^+ and La^{3+} cations on the A site (Supplementary Fig. 16). In ReO_3, WO_3 and LLTO, Li ions occupy 4- and 5-coordinate sites and diffuse through square planar window transition states. It is well established that this process is fast; an activation energy of 120–220 meV is found in LLTO, whose framework is stabilized by the large lanthanum ions[39–45]. By contrast, although ReO_3 and WO_3 should also be suitable for rapid three-dimensional lithium motion, their open and flexible framework can undergo a structural phase transition that locks the Li^+ in place, reducing Li mobility considerably[40].

The shear and bronze structure formation mechanisms result in frustrated polyhedral networks that can no longer undergo tilts upon lithiation that would clamp the lithium ions, preventing their motion. These concepts are well established in perovskites, where the so-called rigid-unit modes drive long-range cooperative distortions despite the framework structure[46,47]. By contrast, crystallographic shear and twisted, locked octahedra (Supplementary Fig. 16) lead to two fundamentally different—but effectively three-dimensional—conduction networks for lithium, while stabilizing the framework and precluding substantial Li-induced rigid-unit mode displacements that lead to local and long-range structural rearrangements.

Structural analyses and bond-valence energy landscape calculations (Extended Data Fig. 9a, b) indicate that infinite lithium diffusion in the $Nb_{16}W_5O_{55}$ block phase is one-dimensional along the b axis, but the twelve parallel tunnels act as a metaphorical multi-lane highway, enabling lithium to change 'lanes' via local hops in the a–c plane. Lithium sites and diffusion in this twelve-channel path may be analogous to those of the ReO_3 and LLTO structure types (Extended Data Fig. 9c), but without the phase transition of ReO_3 or the blocking La^{3+} ions of LLTO. Furthermore, given this mechanism, $Nb_{16}W_5O_{55}$ should not be susceptible to the tunnel-blocking defects that hinder micrometre-sized one-dimensional conductors, such as $LiFePO_4$[48–50]. The $Nb_{18}W_{16}O_{93}$ bronze-like phase has an infinite two-dimensional lithium pathway similarly to high-rate T-Nb_2O_5 in the a–b crystallographic plane, with the additional benefit of four- and five-membered

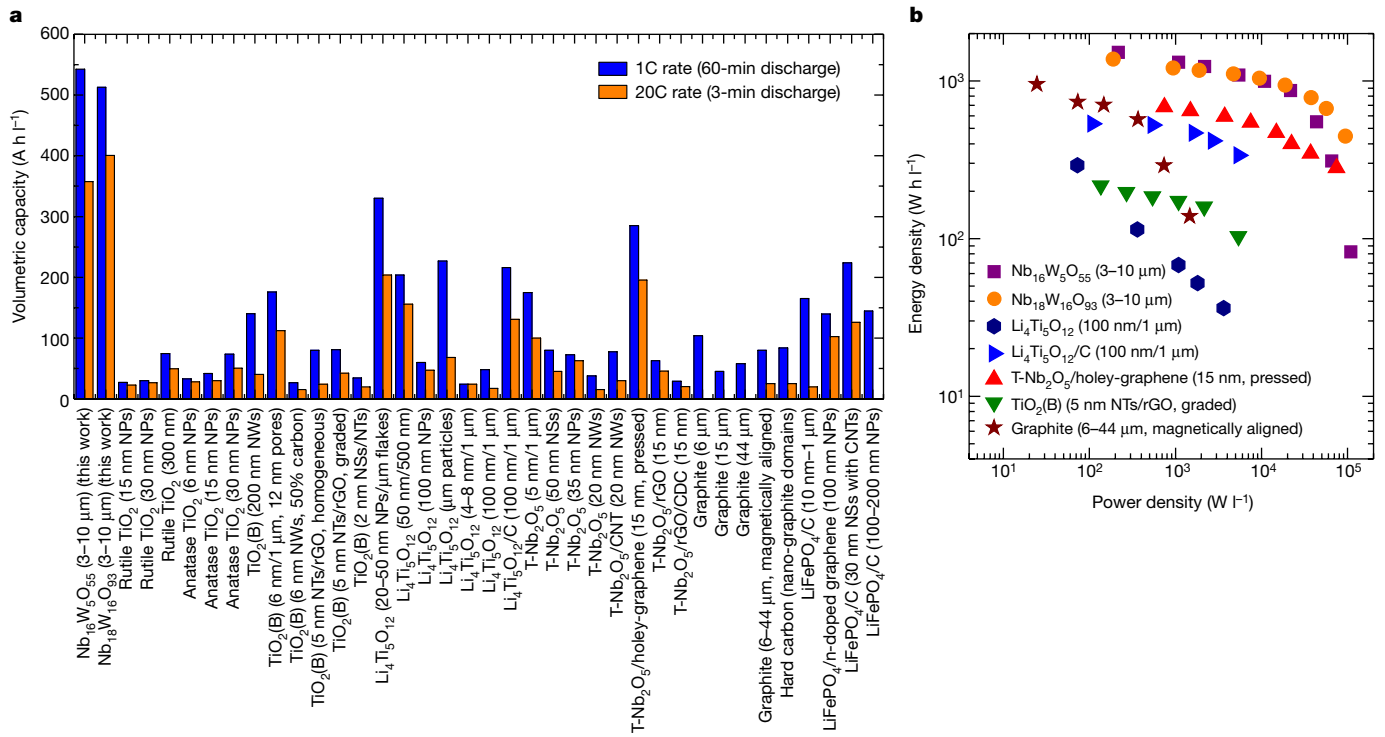

Fig. 5 | Charge, energy, and power densities of micrometre-sized $Nb_{16}W_5O_{55}$ and $Nb_{18}W_{16}O_{93}$ compared to state-of-the-art high-rate nanoscale materials and formulations. a, $Nb_{16}W_5O_{55}$ and $Nb_{18}W_{16}O_{93}$ charge-storage results from this work are compared to high-rate electrode formulations from the literature (see Supplementary Table 2). Volumetric capacities at 1C and 20C are determined from reported capacities and from reported, measured or estimated tap densities (Supplementary Table 2). The sizes of the primary and, where appropriate, secondary particles or pores are indicated. NP, nanoparticle; NW, nanowire; rGO, reduced graphene oxide; NS, nanosheet; NT, nanotube; CDC, carbide-derived carbon; CNT, carbon nanotube. **b**, Ragone (double logarithmic) plot of energy density and power density for anode active materials versus a 4.0-V cathode (Methods and Supplementary Table 2, including relevant literature references). The mass loading of the niobium tungsten oxides was 2.6 mg cm^{-2} and that of the other titanium- and niobium-based materials was about 1 mg cm^{-2}. Graphite is included as a reference, although it suffers from Li plating risks and particle fracture when used at high rates.

windows and channels along the *c* axis to increase the dimensionality of long-range diffusion to three dimensions. As a result, the structure appears to exhibit better performance, certainly under comparable morphologies and conditions, than the recently intensely studied T-Nb_2O_5[11,19,28,51,52]. The bronze comparisons stress the complementary benefits of the open room-and-pillar host structure found in T-Nb_2O_5[11] and $Nb_{18}W_{16}O_{93}$ and the additional perpendicular lithium diffusion channels in $Nb_{18}W_{16}O_{93}$. In addition, both $Nb_{16}W_5O_{55}$ and $Nb_{18}W_{16}O_{93}$ may benefit from the randomly distributed Nb and W occupancy throughout the metal sites, which prevents rate-inhibiting long-range lithium ordering(s). $Nb_{16}W_5O_{55}$ and $Nb_{18}W_{16}O_{93}$ are compared to their binary counterparts H- and T-Nb_2O_5, respectively, as a function of capacity and Li^+/TM (Extended Data Fig. 9d–g). Although the niobium tungsten oxide hosts are d^0 insulators, their three-dimensional –M–O– connectivity enables effective electronic pathways because the structure is n-doped upon lithiation. In addition, variations of the bronze and crystallographic shear structure types are abundant and tunable for specific applications and beyond Li electrochemical energy storage (see Methods for further discussion regarding structure family extensions).

Volumetric energy density and future applications

When compared strictly on the basis of the theoretical 1.0 Li^+/TM reaction and crystallographic density of the active material, titania, niobia and graphite could all display charge densities of greater than 800 A h l^{-1} (Supplementary Fig. 17). Once experimental capacities, multielectron redox and tap density are considered (Fig. 5a, Supplementary Table 2), the bulk, unoptimized niobium tungsten oxides presented here maintain volumetric charge storage densities greater than 500 A h l^{-1} at 1C and up to 400 A h l^{-1} at 20C—performance that even the most optimized versions of TiO_2, Nb_2O_5 and $Li_4Ti_5O_{12}$ cannot achieve. This does not mean that the compounds presented here cannot be improved by methods such as nanostructuring, calendaring or carbon coating (see, for example, ref. [52]), but proves that large, micrometre-sized particles can be used for high-rate electrodes and illustrates that nanoscaling is not always the most appropriate strategy to improve performance. This is evident in a Ragone plot (Fig. 5b), which shows the higher energy and power densities of the new bulk niobium tungsten oxides compared with literature values for state-of-the-art high-rate anode materials and with graphite (see expanded dataset including other electrode materials, details and references in Supplementary Table 2).

The ability to intercalate lithium into microscopic particles in minutes, with transport numbers approaching the best liquid and solid electrolytes, calls for a different paradigm for electrode structuring. Rather than focusing on particle dimensions, other aspects—such as electrolyte transport or counter electrode diffusivity and overpotential—may become more critical to enhancing performance. The strict requirements for carbon coating and intricately wiring nanoparticles are relaxed and issues stemming from surface reactivity and stability are also diminished. Other applications of these materials can be envisaged. For example, in the field of all-solid-state batteries, there has been a mismatch between lithium transport in superionic solid electrolytes compared with electrode materials. If both components have similar diffusivities, it may be possible to design and implement new, simplified composite structures to speed up the realization of safe all-solid-state energy storage.

In conclusion, extremely high-rate performance has been achieved without nanoscaling by identifying appropriate three-dimensional oxide crystal structures. The two new electrode materials, $Nb_{16}W_5O_{55}$ and $Nb_{18}W_{16}O_{93}$, effectively use superstructure motifs to provide stable host structures for lithium intercalation with facile and defect-tolerant

lithium diffusion and multielectron redox. Volume expansion is mitigated by structural contraction along specific crystallographic axes in response to increased lithium content, which may enable the extended cycling of these large particles[53]. The materials investigated here operate in a similar voltage region to the well-studied, and generally considered to be 'safe', anode materials $Li_4Ti_5O_{12}$ and TiO_2(B). In contrast to approaches that try to overcome physical properties (such as ionic and electronic conductivity) extrinsically (for example, by nanoscaling and carbon coating), the high-rate, high-capacity properties of the niobium tungsten oxide block and bronze phases presented here are intrinsic to the complex atomic and electronic networks. The path forward for new fast ionic conductors should consider host structures with open yet frustrated topologies (that prevent structural rearrangements that reduce Li transport) and that also contain 'disorder' in the sense of a multitude of guest sites for Li^+ and limited interaction between the host and guest (that is, no strong coupling between the diffusing Li^+ and associated electron, as found in $LiFePO_4$[54], or between the Li^+ and the host structure itself). This leads to a relatively flat potential energy surface with small kinetic diffusion barriers for Li transport. These criteria, which lead to extremely high power and energy densities (Fig. 5b), are satisfied in $Nb_{16}W_5O_{55}$ and $Nb_{18}W_{16}O_{93}$ via crystallographic shear and pentagonal columns that prop open the framework structures and through transition-metal disorder that prevents Li ordering.

Online content

Any Methods, including any statements of data availability and Nature Research reporting summaries, along with any additional references and Source Data files, are available in the online version of the paper at https://doi.org/10.1038/s41586-018-0347-0.

Received: 26 October 2017; Accepted: 11 June 2018;
Published online 25 July 2018.

1. Zhao, K., Pharr, M., Vlassak, J. J. & Suo, Z. Fracture of electrodes in lithium-ion batteries caused by fast charging. *J. Appl. Phys.* **108**, 073517 (2010).
2. Vetter, J. et al. Ageing mechanisms in lithium-ion batteries. *J. Power Sources* **147**, 269–281 (2005).
3. Downie, L. E. et al. In situ detection of lithium plating on graphite electrodes by electrochemical calorimetry. *J. Electrochem. Soc.* **160**, A588–A594 (2013).
4. Kim, C., Norberg, N. S., Alexander, C. T., Kostecki, R. & Cabana, J. Mechanism of phase propagation during lithiation in carbon-free $Li_4Ti_5O_{12}$ battery electrodes. *Adv. Funct. Mater.* **23**, 1214–1222 (2013).
5. Wang, C. et al. A robust strategy for crafting monodisperse $Li_4Ti_5O_{12}$ nanospheres as superior rate anode for lithium ion batteries. *Nano Energy* **21**, 133–144 (2016).
6. Odziomek, M. et al. Hierarchically structured lithium titanate for ultrafast charging in long-life high capacity batteries. *Nat. Commun.* **8**, 15636 (2017).
7. Oszajca, M. F., Bodnarchuk, M. I. & Kovalenko, M. V. Precisely engineered colloidal nanoparticles and nanocrystals for Li-ion and Na-ion batteries: model systems or practical solutions? *Chem. Mater.* **26**, 5422–5432 (2014).
8. Palacín, M. R., Simon, P. & Tarascon, J. M. Nanomaterials for electrochemical energy storage: the good and the bad. *Acta Chim. Slov.* **63**, 417–423 (2016).
9. Wu, H. et al. Stable cycling of double-walled silicon nanotube battery anodes through solid-electrolyte interphase control. *Nat. Nanotechnol.* **7**, 310–315 (2012).
10. Kasnatscheew, J. et al. A tutorial into practical capacity and mass balancing of lithium ion batteries. *J. Electrochem. Soc.* **164**, A2479–A2486 (2017).
11. Griffith, K. J., Forse, A. C., Griffin, J. M. & Grey, C. P. High-rate intercalation without nanostructuring in metastable Nb_2O_5 bronze phases. *J. Am. Chem. Soc.* **138**, 8888–8899 (2016).
12. Stramare, S., Thangadurai, V. & Weppner, W. Lithium lanthanum titanates: a review. *Chem. Mater.* **15**, 3974–3990 (2003).
13. Shen, L., Zhang, X., Uchaker, E., Yuan, C. & Cao, G. $Li_4Ti_5O_{12}$ nanoparticles embedded in a mesoporous carbon matrix as a superior anode material for high rate lithium ion batteries. *Adv. Energy Mater.* **2**, 691–698 (2012).
14. Prakash, A. S. et al. Solution-combustion synthesized nanocrystalline $Li_4Ti_5O_{12}$ as high-rate performance Li-ion battery anode. *Chem. Mater.* **22**, 2857–2863 (2010).
15. Xu, G. B. et al. Highly-crystalline ultrathin $Li_4Ti_5O_{12}$ nanosheets decorated with silver nanocrystals as a high-performance anode material for lithium ion batteries. *J. Power Sources* **276**, 247–254 (2015).
16. Ren, Y. et al. Nanoparticulate TiO_2(B): an anode for lithium-ion batteries. *Angew. Chem. Int. Ed.* **51**, 2164–2167 (2012).
17. Liu, H. et al. Mesoporous TiO_2–B microspheres with superior rate performance for lithium ion batteries. *Adv. Mater.* **23**, 3450–3454 (2011).
18. Beuvier, T. et al. TiO_2(B) nanoribbons as negative electrode material for lithium ion batteries with high rate performance. *Inorg. Chem.* **49**, 8457–8464 (2010).
19. Augustyn, V. et al. High-rate electrochemical energy storage through Li^+ intercalation pseudocapacitance. *Nat. Mater.* **12**, 518–522 (2013).
20. Liu, X. et al. Urchin-like hierarchical H-Nb_2O_5 microspheres: synthesis, formation mechanism and their applications in lithium ion batteries. *Dalton Trans.* **46**, 10935–10940 (2017).
21. Lai, C.-H. et al. Designing pseudocapacitance for Nb_2O_5/carbide-derived carbon electrodes and hybrid devices. *Langmuir* **33**, 9407–9415 (2017).
22. Roth, R. S. & Waring, J. L. Phase equilibria as related to crystal structure in the system niobium pentoxide–tungsten trioxide. *J. Res. Natl Bur. Stand.* **70A**, 281–303 (1966).
23. Roth, R. S. & Wadsley, A. D. Multiple phase formation in the binary system Nb_2O_5–WO_3. II. The structure of the monoclinic phases $WNb_{12}O_{33}$ and $W_5Nb_{16}O_{55}$. *Acta Crystallogr.* **19**, 32–38 (1965).
24. Roth, R. S. & Wadsley, A. D. Multiple phase formation in the binary system Nb_2O_5–WO_3. I. Preparation and identification of phases. *Acta Crystallogr.* **19**, 26–32 (1965).
25. Stephenson, N. C. A structural investigation of some stable phases in the region Nb_2O_5·WO_3–WO_3. *Acta Crystallogr. B* **24**, 637–653 (1968).
26. Naoi, K., Ishimoto, S., Isobe, Y. & Aoyagi, S. High-rate nano-crystalline $Li_4Ti_5O_{12}$ attached on carbon nano-fibers for hybrid supercapacitors. *J. Power Sources* **195**, 6250–6254 (2010).
27. Cava, R. J., Murphy, D. W. & Zahurak, S. M. Lithium insertion in Wadsley–Roth phases based on niobium oxide. *J. Electrochem. Soc.* **130**, 2345–2351 (1983).
28. Kumagai, N., Koishikawa, Y., Komaba, S. & Koshiba, N. Thermodynamics and kinetics of lithium intercalation into Nb_2O_5 electrodes for a 2 V rechargeable lithium battery. *J. Electrochem. Soc.* **146**, 3203–3210 (1999).
29. Patoux, S., Dolle, M., Rousse, G. & Masquelier, C. A Reversible lithium intercalation process in an ReO_3 type structure PNb_9O_{25}. *J. Electrochem. Soc.* **149**, A391–A400 (2002).
30. Han, J.-T., Huang, Y.-H. & Goodenough, J. B. New anode framework for rechargeable lithium batteries. *Chem. Mater.* **23**, 2027–2029 (2011).
31. Saritha, D., Pralong, V., Varadaraju, U. V. & Raveau, B. Electrochemical Li insertion studies on $WNb_{12}O_{33}$—a shear ReO_3 type structure. *J. Solid State Chem.* **183**, 988–993 (2010).
32. Griffith, K. J., Senyshyn, A. & Grey, C. P. Structural stability from crystallographic shear in TiO_2–Nb_2O_5 phases: cation ordering and lithiation behavior of $TiNb_{24}O_{62}$. *Inorg. Chem.* **56**, 4002–4010 (2017).
33. Roberts, M. R. et al. Direct observation of active material concentration gradients and crystallinity breakdown in $LiFePO_4$ electrodes during charge/discharge cycling of lithium batteries. *J. Phys. Chem. C* **118**, 6548–6557 (2014).
34. Strobridge, F. C. et al. Unraveling the complex delithiation mechanisms of olivine-type cathode materials, $LiFe_xCo_{1-x}PO_4$. *Chem. Mater.* **28**, 3676–3690 (2016).
35. Mary, T. A., Evans, J. S. O., Vogt, T. & Sleight, A. W. Negative thermal expansion from 0.3 to 1050 Kelvin in ZrW_2O_8. *Science* **272**, 90–92 (1996).
36. Lin, K. et al. Ordered structure and thermal expansion in tungsten bronze $Pb_2K_{0.5}Li_{0.5}Nb_5O_{15}$. *Inorg. Chem.* **53**, 9174–9180 (2014).
37. Cairns, A. B. & Goodwin, A. L. Negative linear compressibility. *Phys. Chem. Chem. Phys.* **17**, 20449–20465 (2015).
38. Liu, H. et al. Intergranular cracking as a major cause of long-term capacity fading of layered cathodes. *Nano Lett.* **17**, 3452–3457 (2017).
39. Murphy, D. W., Greenblatt, M., Cava, R. J. & Zahurak, S. M. Topotactic lithium reactions with ReO_3 related shear structures. *Solid State Ion.* **5**, 327–329 (1981).
40. Cava, R. J., Santoro, A., Murphy, D. W., Zahurak, S. M. & Roth, R. S. The structures of the lithium inserted metal oxides $Li_{0.2}ReO_3$ and $Li_{0.36}WO_3$. *J. Solid State Chem.* **50**, 121–128 (1983).
41. Gracia, L. et al. Composition dependence of the energy barrier for lithium diffusion in amorphous WO_3. *Electrochem. Solid State Lett.* **8**, J21–J23 (2005).
42. Shan, Y. J., Inaguma, Y. & Itoh, M. The effect of electrostatic potentials on lithium insertion for perovskite oxides. *Solid State Ion.* **79**, 245–251 (1995).
43. Chen, C. & Du, J. Lithium ion diffusion mechanism in lithium lanthanum titanate solid-state electrolytes from atomistic simulations. *J. Am. Ceram. Soc.* **98**, 534–542 (2015).
44. Jay, E. E., Rushton, M. J. D., Chroneos, A., Grimes, R. W. & Kilner, J. A. Genetics of superionic conductivity in lithium lanthanum titanates. *Phys. Chem. Chem. Phys.* **17**, 178–183 (2015).
45. Emery, J., Buzare, J. Y., Bohnke, O. & Fourquet, J. L. Lithium-7 NMR and ionic conductivity studies of lanthanum lithium titanate electrolytes. *Solid State Ion.* **99**, 41–51 (1997).
46. Giddy, A. P., Dove, M. T., Pawley, G. S. & Heine, V. The determination of rigid-unit modes as potential soft modes for displacive phase transitions in framework crystal structures. *Acta Crystallogr. A* **49**, 697–703 (1993).
47. Dove, M. T., Trachenko, K. O., Tucker, M. G. & Keen, D. A. Rigid unit modes in framework structures: theory, experiment and applications. *Rev. Mineral. Geochem.* **39**, 1–33 (2000).
48. Islam, M. S., Driscoll, D. J., Fisher, C. A. J. & Slater, P. R. Atomic-scale investigation of defects, dopants, and lithium transport in the $LiFePO_4$ olivine-type battery material. *Chem. Mater.* **17**, 5085–5092 (2005).
49. Dathar, G. K. P., Sheppard, D., Stevenson, K. J. & Henkelman, G. Calculations of Li-ion diffusion in olivine phosphates. *Chem. Mater.* **23**, 4032–4037 (2011).
50. Liu, H. et al. Effects of antisite defects on Li diffusion in $LiFePO_4$ revealed by Li isotope exchange. *J. Phys. Chem. C* **121**, 12025–12036 (2017).
51. Zhang, C. et al. Synthesis and charge storage properties of hierarchical niobium pentoxide/carbon/niobium carbide (MXene) hybrid materials. *Chem. Mater.* **28**, 3937–3943 (2016).

52. Sun, H. et al. Three-dimensional holey-graphene/niobia composite architectures for ultrahigh-rate energy storage. *Science* **356**, 599–604 (2017).
53. Zhang, S. Chemomechanical modeling of lithiation-induced failure in high-volume-change electrode materials for lithium ion batteries. *Npj Comput. Mater.* **3**, 7 (2017).
54. Maxisch, T., Zhou, F. & Ceder, G. Ab initio study of the migration of small polarons in olivine Li_xFePO_4 and their association with lithium ions and vacancies. *Phys. Rev. B* **73**, 104301 (2006).

Acknowledgements K.J.G. acknowledges support from The Winston Churchill Foundation of the United States, a Herchel Smith Scholarship and a Science and Technology Facilities Council Futures Early Career Award. K.J.G. and C.P.G. thank the EPSRC for a LIBATT grant (EP/M009521/1). L.E.M. acknowledges support from the European Union's Horizon 2020 research and innovation programme under the Marie Skłodowska–Curie grant agreement number 750294 and a Charles and Katharine Darwin Research Fellowship. We thank I. Seymour from the University of Cambridge and B. Dunn from the University of California, Los Angeles for fruitful discussions. We thank J. Skepper and H. Greer from the University of Cambridge for assistance with electron microscopy and M. Avdeev from the Bragg Institute for the bond valence sum mapping program. We thank O. Borkiewicz from the Advanced Photon Source at Argonne National Laboratory and A. Kasam from the University of Cambridge for diffraction data reduction scripts. We thank Diamond Light Source for access to beamline B18 (SP11433, SP14956, SP16387, SP17913), where we obtained results presented here. This research used resources of the Advanced Photon Source (GUP40466, GUP41657, GUP47967), a US Department of Energy (DOE) Office of Science User Facility operated for the DOE Office of Science by Argonne National Laboratory under contract number DE-AC02-06CH11357.

Reviewer information *Nature* thanks S. Greenbaum, P. Woodward and the other anonymous reviewer(s) for their contribution to the peer review of this work.

Author contributions K.J.G. and C.P.G. conceived the idea. K.J.G. synthesized and characterized the materials and performed the electrochemistry experiments. K.J.G. performed the synchrotron diffraction and absorption experiments and analysed the data with support from K.M.W. and G.C. L.E.M. and K.J.G. performed the PFG NMR measurements. K.J.G. and C.P.G. wrote the manuscript with input from all co-authors.

Competing interests K.J.G. and C.P.G., via Cambridge Enterprise, have filed a UK patent application (GB1809467.2) covering the materials and high-rate energy storage application described in this manuscript.

Additional information
Extended data is available for this paper at https://doi.org/10.1038/s41586-018-0347-0.
Supplementary information is available for this paper at https://doi.org/10.1038/s41586-018-0347-0.

Correspondence and requests for materials should be addressed to C.P.G.

METHODS

Synthesis and structure characterization. $Nb_{16}W_5O_{55}$ and $Nb_{18}W_{16}O_{93}$ were synthesized by co-thermal oxidation of dark-blue NbO_2 (Alfa Aesar, 99+%) and brown WO_2 (Alfa Aesar, 99.9%) in batches of approximately 1–5 g. The partially reduced oxides were massed to within 0.001 g of the 16:5 or 18:16 stoichiometric ratios, ground together by hand with an agate mortar and pestle, pressed into a pellet at 10 MPa, heated in a platinum crucible at a rate of 10 K min^{-1} to 1,473 K, and naturally cooled in the furnace over approximately 2 h. Both phases formed subhedral particles with approximately 3–10-μm primary particles that appeared in the electron microscope to be intergrown/'cemented' into larger secondary particles of around 10–30 μm (Fig. 1, Supplementary Fig. 3a, b). As synthesized, $Nb_{16}W_5O_{55}$ is pale yellow–green and $Nb_{18}W_{16}O_{93}$ is off-white (Supplementary Fig. 3c) (we note that the colours of both mixed metal oxides are between those of light-green WO_3 and white Nb_2O_5). Energy-dispersive X-ray spectroscopy (EDX) revealed a uniform distribution of niobium, tungsten and oxygen, with no apparent phase-segregated particles and no presence of any other elements (besides those on the background adhesive carbon) (Supplementary Figs. 4, 5). We note that although phases such as Nb_2O_5 and WO_3 would be distinct via EDX, particles of niobium tungsten oxide phases with similar composition to that of $Nb_{16}W_5O_{55}$ or $Nb_{18}W_{16}O_{93}$ would not be distinguishable. Although the phase diagram[55] suggests that $Nb_{16}W_5O_{55}$ is only formed at about 1,363–1,658 K and is a metastable phase that should disproportionate to $Nb_{14}W_3O_{44}$ and Nb_2WO_8 on cooling, this was not observed. $Nb_{16}W_5O_{55}$ retains its high-temperature structure on quenching[56] and even with more modest cooling. In the original synthetic report[24], Roth and Wadsley also noted that phase-pure $Nb_{16}W_5O_{55}$ was obtained even after annealing at 1,273 K for one to three days after an initial heat treatment at 1,623 K for 24 h. To investigate other synthetic methods, samples were also prepared by quenching the samples from 1,473 K onto a steel plate, as well as from analogous pellets or loose mixed powders of Nb_2O_5 (Alfa Aesar, 99.9985%, H-phase) and WO_3 (Sigma-Aldrich, ≥99%, γ-phase) precursors. Large (20 g) single batches of $Nb_{16}W_5O_{55}$ and $Nb_{18}W_{16}O_{93}$ were produced by hand grinding (agate, 5 min) or ball milling (SPEX 8000M high-energy mixer/mill; zirconia jar with two 5-g zirconia balls, 90 min) Nb_2O_5 and WO_3 powder, followed by heating in a platinum crucible covered with a platinum lid in air at 973 K for 12 h and then at 1,473 K for 12 h. The large batches were heated at 10 K min^{-1} and the samples were allowed to cool naturally in the furnace over about 2 h. Thermogravimetric analysis (TGA, Supplementary Fig. 6) revealed that WO_2 oxidizes to WO_3 starting at around 700 K and NbO_2 oxidizes to Nb_2O_5 starting at around 550 K. At 1,273 K, the WO_2 sample had gained 7.8% mass versus the expected 7.4%, and NbO_2 had gained 5.8% compared to the expected 6.4%. These small differences may arise from slight off-stoichiometry in the starting material. WO_3 undergoes sublimation at temperatures near or above 1,273 K; however, the reaction with niobium oxide apparently stabilizes the volatile tungsten to considerably higher temperatures. After 24 h at 1,473 K, the mass change was –0.4% for $Nb_{16}W_5O_{55}$ and –0.3% for $Nb_{18}W_{16}O_{93}$ compared with the expected values, which is within the error of the expected mass changes for NbO_2 and WO_2 oxidation.

Laboratory powder X-ray diffraction patterns were measured at ambient temperature with a Cu Kα source in Bragg–Brentano geometry at a scan rate of 0.83° min^{-1}. The sample stage rotated continuously to improve powder averaging. Sample phase and purity were determined by Rietveld refinement in GSAS-II (Supplementary Fig. 7)[57]. Given the synthesis time and temperature (24 h and 1,473 K), the block-phase $Nb_{16}W_5O_{55}$ samples are expected to contain several per cent of Wadsley defect fringes, as suggested by the laborious study of Allpress and Roth[58].

TGA measurements were performed on a Mettler Toledo TGA/SDTA 851 thermobalance. Samples were placed in a tared 100-μl alumina crucible and the mass was recorded from 323 K to 1,273 K in steps of 1 K min^{-1} under a constant air flow (50 ml min^{-1}). A blank with an empty crucible was recorded under the same conditions and subtracted from the NbO_x/WO_x data. The raw data were numerically differentiated to obtain differential thermogravimetry curves.

Scanning electron microscopy images were taken with a Sigma VP instrument (Zeiss) at 3.0 kV and a MIRA3 instrument (TESCAN) at 5.0 kV with secondary-electron detection.

Tap density was recorded on an AutoTap (Quantachrome Instruments) instrument operating at 257 taps per minute. Tap densities were measured according to the ASTM international standard B527-15, modified to accommodate a 5–10 cm^3 graduated cylinder.

Electrochemical characterization. All electrochemical measurements were conducted in stainless-steel 2032 coin cells (Cambridge Energy Solutions) with a stainless-steel conical spring, two 0.5-mm-thick stainless-steel spacer disks, a plastic gasket and a glass microfibre separator (Whatman). The electrode had an active material:carbon:binder mass ratio of 8:1:1, active material loading of 2–3 mg cm^{-2} and an area of 1.27 cm^2. The metal oxide and conductive carbon (Super P, TIMCAL) were ground by hand in an agate mortar and pestle in an 8:1 mass ratio. This powder was ground in a 9:1 mass ratio with poly(vinylidene difluoride) (PVDF, Kynar) dispersed in *N*-methyl pyrrolidone (NMP; Sigma-Aldrich, anhydrous, 99.5%). Although standard, SuperP carbon is a nanoparticulate powder and NMP is a hazardous organic solvent, so appropriate nanoparticle cabinets and fume hoods should be used. This metal oxide/carbon/polymer electrode served as the cathode against a Li metal-disk (LTS Research, 99.95%) anode in half-cell geometry. The electrolyte for all experiments was 1.0 M $LiPF_6$ dissolved in 1:1 v/v ethylene carbonate/dimethyl carbonate (EC/DMC; Sigma-Aldrich, battery grade). No additives were used. Electrochemistry measurements were performed in a temperature-controlled room at 293 ± 2 K. A galvanostat/potentiostat (BioLogic) with EC-Laboratory software was used to perform the electrochemical measurements. All potentials are reported with respect to Li^+/Li^0.

In this work, the C-rate is always defined relative to one-electron transfer per transition metal; for example, for $Nb_{16}W_5O_{55}$, 1C = 171.3 mA g^{-1} and 20C = 3,426 mA g^{-1}. Theoretical capacity is calculated by:

$$Q_{\text{theoretical}} = \frac{nF}{3.6m} = \frac{21 \times 96{,}485.3 \text{ C mol}^{-1}}{3.6 \text{ C mA}^{-1}\text{ h}^{-1} \times 3{,}285.65 \text{ g mol}^{-1}} = 171.3 \text{ mA h g}^{-1}$$

where n is the number of electrons transferred per formula unit, F is Faraday's constant, 3.6 is a conversion factor between coulombs and the conventional milliampere-hour and m is the mass per formula unit.

In a Ragone plot[59], the energy density of a battery cathode material or full cell is the product of capacity (Q) and voltage (V); however, this quantity is not appropriate when comparing anode materials, where energy and voltage have an inverse relationship. In the calculation of the anode-material Ragone plot in Fig. 5b, the energy (E) is computed on the basis of the voltage difference versus a 4.0-V cathode. Thus, normalized to the anode, $E_{\text{anode}} = Q_{\text{anode}}(V_{\text{cathode}} - V_{\text{anode}})$. Literature values for the Ragone plot were extracted with WebPlotDigitizer[60].

Operando synchrotron X-ray diffraction. Operando powder diffraction measurements were carried out at beamline 17BM (bending magnet) at the Advanced Photon Source at Argonne National Laboratory. The samples were measured at ambient temperature in transmission geometry at 17.0 keV (0.7295 Å or 0.72768 Å) with an area detector. All operando measurements were performed in the AMPIX cell, which has been described elsewhere[61]. In brief, it contains a hard, conductive glassy carbon window to prevent inhomogeneous electrochemical reactions, which are a concern with flexible or non-conductive X-ray windows[61]. Owing to the absorbing nature of niobium and tungsten and the absence of a current collector, self-standing electrodes were made with a 3:6:1 ($Nb_{16}W_5O_{55}$ at C/2) or 5:4:1 ($Nb_{16}W_5O_{55}$ at 5C and $N_{18}W_{16}O_{93}$ at 1C, 5C and 10C) mass ratio of metal oxide:SuperP carbon:poly(tetrafluoroethylene). The resulting electrodes were approximately 1.0 cm in diameter and contained 5.3 mg, 8.7 mg and 8.0 mg of active material for $Nb_{16}W_5O_{55}$ (C/2), $Nb_{16}W_5O_{55}$ (5C) and $N_{18}W_{16}O_{93}$ (1C, 5C and 10C), respectively. These electrodes correspond to areal metal-oxide mass loadings of 6.8–11.1 mg cm^{-2}. AMPIX cells were constructed in an argon glovebox with lithium-metal counter-electrodes, glass-fibre separators (Whatman) and 1.0 M $LiPF_6$ dissolved in 1:1 v/v ethylene carbonate/diethyl carbonate (EC/DEC). Two-dimensional image data were converted to conventional one-dimensional diffraction patterns through integration in GSAS-II after calibration with LaB_6[57]. Background subtraction, primarily from the glassy carbon window, and normalization to incident X-ray intensity were performed on the one-dimensional integrated diffraction data.

Sequential Rietveld refinement of the unit-cell parameters of $Nb_{16}W_5O_{55}$ and $Nb_{18}W_{16}O_{93}$ during operando galvanostatic electrochemical lithiation was performed in GSAS-II. The initial structure model was based on Rietveld refinement of the atomic coordinates, unit-cell parameters, background, zero offset and peak-shape parameters (U, V and W; peak width squared (H^2) = $U\tan^2\theta + V\tan\theta + W$)[62] of the first in situ diffraction pattern before the application of a current. For the sequential refinement, only the unit-cell parameters and Chebyshev background coefficients were allowed to vary. Refinement of the atomic coordinates was not attempted owing to the large number of variables this would introduce, the weak relative scattering of lithium and oxygen versus niobium and tungsten, and the optimization of experiments towards rapid data collection. $Nb_{16}W_5O_{55}$ contains 11 metal sites and 28 oxygen sites and $Nb_{18}W_{16}O_{93}$ contains 10 metal sites and 25 oxygen sites in the asymmetric unit. Two-dimensional diffraction images (integrated to one-dimensional patterns) were collected in 7–15 s (Supplementary Table 3).

$Nb_{18}W_{16}O_{93}$, which exhibits a region of two-phase behaviour, was fitted using a double-ended sequential Rietveld refinement, in which the process described above was also initiated from the structure at the end of the discharge and a 'backward' refinement was performed. Error bars (Extended Data Fig. 5) are derived from the refinements. The unit-cell parameters in the two-phase region of $Nb_{18}W_{16}O_{93}$ and the inhomogeneous solid-solution region of $Nb_{16}W_5O_{55}$ were estimated by fitting individual reflections to two sets of lattice parameters ($Nb_{18}W_{16}O_{93}$) and measuring the range of individual reflections ($Nb_{16}W_5O_{55}$); thus, error bars in these

regions cannot be calculated using the whole pattern-refinement method. Owing to the unit-cell dimensions and pseudosymmetry, there is severe overlap of reflections in the powder diffraction patterns of both $Nb_{18}W_{16}O_{93}$ and $Nb_{16}W_5O_{55}$, even at the high resolution available at a synchrotron X-ray source. Furthermore, anisotropic lattice expansion results in reflections crossing during discharge (Fig. 4), which introduces challenges for sequential refinement. At 145–155 mA h g^{-1} in $Nb_{16}W_5O_{55}$, this crossover (Fig. 4a, Extended Data Fig. 6k) resulted in strongly correlated and inconsistent fits for four consecutive diffraction patterns. These patterns were fitted according to the individual reflection model described above assuming linear changes—an approximation over the small change in lithium content and unit-cell dimensions.

For the crystallographic shear structure with monoclinic symmetry ($Nb_{16}W_5O_{55}$; Fig. 1a, Fig. 4c), the *b* axis represents the 'layered' direction and the 'block area' is parameterized by $ac\sin\beta$, where the *a* and *c* axes define the plane of the block and β is the angle between *a* and *c*. The unit-cell volume of this phase is the product of the block area and the layer spacing, $(ac\sin\beta)b$. For the bronze-like phase with orthorhombic symmetry ($Nb_{18}W_{16}O_{93}$, Fig. 1d, Fig. 4d), the unit-cell volume is simply the product of the crystallographic axes, *abc*.

Operando and ex situ synchrotron X-ray absorption spectroscopy. Operando X-ray absorption spectroscopy (XAS) was performed at beamline 9BM (bending magnet) at the Advanced Photon Source at Argonne National Laboratory. Nb K edge spectra were recorded at ambient temperature in transmission mode above and below the absorption edge of 18,986 eV. The same AMPIX cells were used as for the diffraction measurements, but with a higher metal-oxide loading of 22.5 mg and lower carbon content (8:1:1 ratio of oxide:carbon:binder) at C/3.

Ex situ XAS was performed at beamline B18 (bending magnet) at the Diamond Light Source. Spectra of the Nb K edge, W L_I, L_{II} and L_{III} edges were measured at ambient temperature in transmission mode using energy scans above and below the absorption edges of 18,986 eV, 12,100 eV, 11,544 eV and 10,207 eV, respectively. The X-ray energy ranges were scanned over 1,000 eV (W $L_I + L_{II}$) or 1,500 eV (Nb K, W L_{III}) in steps of about 0.4 eV. To synthesize powders for ex situ characterization, pure $Nb_{16}W_5O_{55}$ powder was pressed into pellets at 1–2 MPa, discharged to the relevant lithium content in coin cells as previously described, then extracted in an argon glovebox where it was rinsed three times with 2 ml DMC (Sigma-Aldrich, anhydrous, ≥99%) and hand-ground (agate) back into powder. Upon lithiation, the colour of $Nb_{16}W_5O_{55}$ changed from a pale yellow–green to light blue, then to dark blue, and through to dark maroon above approximately 0.5 Li^+/TM. Samples for XAS were prepared in an argon glovebox by carefully grinding the active material (typically 15–18 mg) with dried cellulose (to a total mass of 60 ± 5 mg) in an agate mortar and pestle to achieve a fine homogeneous sample with a change in absorption coefficient of about 1 across the Nb K and W L_{III} absorption edges. The thoroughly ground powders were pressed into 8-mm-diameter pellets (about 1 mm thick) in the glovebox. Non-air-sensitive samples (pristine and reference) were measured in air and lithiated samples were transferred from the glovebox in a custom-built (Diamond Light Source) transfer chamber with X-ray-transparent windows. The argon in the chamber was flushed with helium to reduce background absorption of the incident X-rays and the samples were measured at a slight overpressure of helium to ensure the exclusion of air. Multiple spectra were collected from each sample to improve the signal-to-noise ratio and to ensure sample stability with respect to possible air contamination or beam damage. The oxides appeared to be stable; no changes were observed for any sample between the first and last measurement (typically 2–6 spectra per sample per absorption edge) over several hours in the sample chamber and 30–60 min in the X-ray beam.

For all XAS measurements, simultaneous measurement of a reference Nb or W foil was performed with each spectrum to ensure X-ray beam stability and for energy calibration. Data merging, calibration/alignment, analysis and peak fitting were performed within the Athena program in the Demeter package running IFEFFIT[63,64]. The Nb K edge, W L_I, L_{II} and L_{III} edges were calibrated to the reference Nb and W metal foils by setting the first maximum in the derivative plot of absorption versus energy equal to the standard electron binding energy[65]. The $Nb_{16}W_5O_{55}$ operando calibration was set to be equivalent to the ex situ calibration to simultaneously compare edge shifts of both datasets.

XAS of the Nb K edge probes excitations from 1*s* to 5*p* at energies around 19,000 eV, which is well suited for standard synchrotron analysis. In principle, the same type of analysis could be performed with excitations from 1*s* to 6*p* at the W K edge, but at 69,500 eV, it is impractically high in energy for standard beamline configurations and suffers from severe core-hole lifetime broadening[66]. The W L edges, however, at 12,100–10,200 eV are suitable for high-resolution XAS. The W L_I edge measures 2*s* to 6*p* excitations whereas the W L_{II} and L_{III} edges correspond to transitions of 2*p* to (near-)valence 5*d* states. The L_{II} and L_{III} edges are split by about 1,337 eV by spin–orbit coupling; in the octahedral sites present in $Nb_{16}W_5O_{55}$, these edges are further split by about 4 eV by ligand-field effects into transitions to t_{2g} and e_g orbitals. Recent studies have demonstrated the use of the 5*d* L_I edges for oxidation-state analysis in periodic[11] and molecular[67,68] structures. We considered this; however, the edge position of the W L_I edge in $Nb_{16}W_5O_{55}$ is severely complicated by the strong pre-edge feature. In this system, the L_{II} edge offered an excellent alternative, with a stronger signal and a single contribution from excitations from $2p_{1/2}$ to $5d_{3/2}$. We note that the contribution expected for 2*p* to 6*s* transitions can be neglected at the absorption edge for early-third-row transition metals[69]. Meanwhile, the W L_I pre-edge peaks that are problematic for energy calibration provide direct evidence for local geometry around the tungsten ions.

An SOJT distortion moves Nb^{5+} and W^{6+} off-centre in the otherwise centrosymmetric environments of the octahedral MO_6 transition-metal sites in $Nb_{16}W_5O_{55}$ and $Nb_{18}W_{16}O_{93}$. The SOJT results from the vibronic mixing of non-degenerate electronic states under nuclear displacements[70]. In a d^0 metal oxide, the energy difference between the ground and excited states is small owing to the pseudodegeneracy of the filled valence *p* orbitals and empty *d* orbitals in the first excited state. This off-centre distortion enables mixing of the dipole-transition-allowed *p* states (for example, 5*p* for the Nb K edge) with lower-energy *d* states (4*d* for the Nb K edge), which gives rise to a pre-edge feature before the main absorption edge in the XAS spectra of the Nb K and W L_I edges and serves as a direct probe of local symmetry and an additional measure of the oxidation state. As the d^0 cations are reduced, the energy of the *d* states moves up and the SOJT distortion is reduced, which increases the local octahedral symmetry and decreases the pre-edge states and intensity. X-ray absorption pre-edge features are well known in tetrahedral and other noncentrosymmetric local-coordination environments, so the SOJT distortion and d^0 electronic configuration are not prerequisites for pre-edge peak intensity from those sites. $Nb_{16}W_5O_{55}$ has 40 distorted octahedral sites and 2 tetrahedral sites per unit cell whereas $Nb_{18}W_{16}O_{93}$ has 30 octahedral sites and 4 occupied pentagonal bipyramidal sites per unit cell, so some pre-edge intensity may be expected, even beyond lithiation to the d^1 electronic configuration. Interestingly, it has been shown that the tetragonal bronze structure cannot be constructed from identical, regular octahedra[71], so some local distortion is topologically required regardless of the oxidation state or SOJT.

We note that for the related shear-phase $Nb_{12}WO_{33}$, the three observed electrochemical regions have tentatively been assigned to the sequential reduction of $W^{6+/5+}$, $Nb^{5+/4+}$ and $Nb^{4+/3+}$ on discharge, but these proposed oxidation changes have not been experimentally verified[31,72].

^{7}Li PFG NMR spectroscopy. ^{7}Li NMR diffusion spectra were recorded on a Bruker Avance III 300 MHz (7.0 T) spectrometer using a Diff50 probe head equipped with an extended variable-temperature 5-mm single-tuned ^{7}Li saddle coil insert. All of the materials examined here had spin–lattice (T_1) relaxation times greater than spin–spin (T_2) relaxation times. Therefore, spectra were recorded with the stimulated-echo PFG sequence shown in Extended Data Fig. 2b to minimize T_2 losses. After the first 90° radiofrequency pulse, the net magnetization loses coherence owing to T_2 relaxation; thus, the time period following this pulse, which includes the first PFG pulse (to encode spin position), must be shorter than T_2. In the stimulated-echo sequence used here, a second 90° radiofrequency pulse was applied to store the net magnetization along the *z* axis, allowing diffusion times, Δ, commensurate with the comparatively longer T_1 value, as no T_2 relaxation occurred. During Δ, a short spoiler gradient (SINE.100) was applied to remove residual transverse magnetization. Afterwards, a third 90° radiofrequency pulse was applied, followed by a PFG pulse to decode the spin position. Sufficiently long delays (1 ms) were used between PFG and radiofrequency pulses to minimize eddy currents in the diffusion measurements.

During this sequence, the gradient strength, *g*, was varied from 0.87 to 1,800 or 2,300 G cm^{-1}, and 16 gradient steps were acquired using 'opt'-shaped pulses with 1,024–4,096 transients. The opt shape is a composite pulse that starts with a quarter of a sine wave, followed by a constant gradient, and ends with a ramp down (Extended Data Fig. 2b). The opt gradient pulses provided the largest gradient integral for a given time period, maximizing the range of diffusion coefficients that we could assess in this experiment.

Spectra were analysed in phase-sensitive mode and the response of the integrated NMR signal intensity, *I*, to variation in *g* is described by the Stejskal–Tanner equation[73]:

$$\frac{I}{I_0} = \exp\left[-g^2\gamma^2\delta^2\left(\Delta - \frac{\delta}{3}\right)D\right]$$

where I_0 is the intensity in the absence of gradients, γ is the gyromagnetic ratio ($\gamma_{^7Li} = 103.962 \times 10^6$ s^{-1} T^{-1}), δ is the effective gradient pulse duration and *D* is the diffusion coefficient. Typical δ values ranged from 0.8 ms to 1.5 ms and Δ values were 50–150 ms for the bronze- and the block-phase samples, respectively.

Diffusion spectra were recorded at elevated temperatures owing to the increase in T_2 observed at high temperature (for example, T_2 for $Li_{3.4}Nb_{18}W_{16}O_{93}$ is approximately 700 μs at room temperature and 1.9 ms at 453 K). (No attempt was made to calibrate the temperature for this experimental setup because a single-tuned ^{7}Li coil was used and no reliable ^{7}Li reference is routinely used for

temperature calibration. The Bruker manual states that for static measurements, the temperature calibration should be within ±7 K of the set value.) The increase in T_2 allowed the use of longer gradient pulses, δ, that were necessary to measure diffusion coefficients in the solid oxides.

Representative ^{7}Li diffusion decay curves for the five samples studied, $Li_xNb_{16}W_5O_{55}$ ($x = 6.3$, 8.4) and $Li_xNb_{18}W_{16}O_{93}$ ($x = 3.4$, 6.8, 10.2), and a representative one-dimensional ^{7}Li NMR spectrum are shown in Extended Data Fig. 2.

Concerning the difficulties associated with measuring self-diffusion coefficients with PFG NMR spectroscopy, it is worth noting that even if the T_2 of these materials was sufficiently long, the cumulative length of δ applied before Δ in the pulse sequence of choice (Extended Data Fig. 2b) should not exceed 5 ms to mitigate probe damage. The limitation of cumulative $\delta = 5$ ms places an inherent limitation on the diffusion coefficients that can be extracted using PFG NMR spectroscopy and effectively places the burden on the length of T_1, which determines the length of Δ.

The PFG data were initially fitted with a single exponential to extract the diffusion coefficients. In the case of the block phase, $Li_{6.3}Nb_{16}W_5O_{55}$, fitting the data with two components for biexponential decay resulted in an improvement (on average) of a factor of two in the residual sum of squares of the fit to the PFG data. Therefore, the ^{7}Li NMR signal of the $Li_{6.3}Nb_{16}W_5O_{55}$ sample presented in Table 1 can be interpreted as consisting of two Li species, one that diffuses rapidly and one that diffuses more slowly (we note that both diffusion coefficients are markedly faster than those reported for $Li_4Ti_5O_{12}$ and $LiFePO_4$). For the higher-Li-content block phase, $Li_{8.4}Nb_{16}W_5O_{55}$, the data were fitted well by a single-component exponential that yielded a similar diffusion coefficient and activation energy to the majority lithium phase in $Li_{6.3}Nb_{16}W_5O_{55}$. This suggests that within the two-component model, the fastest diffusing phase is present at lower lithium concentrations, and by the second stage of the electrochemical profile the structure is composed entirely of the phase with room-temperature lithium diffusion of about 1.6×10^{-13} m^2 s^{-1}.

For all measured stages of lithiation for the bronze phase ($Li_{3.4}Nb_{18}W_{16}O_{93}$, $Li_{6.8}Nb_{18}W_{16}O_{93}$ and $Li_{10.2}Nb_{18}W_{16}O_{93}$), the data were fitted well by a single-component exponential decay (as reflected in the error bars in Extended Data Fig. 2a, which represent 2σ values obtained from the fit), and no remarkable improvement was observed upon fitting by a biexponential.

Linear fits of the ^{7}Li diffusion coefficients of both the block and bronze phases as a function of temperature allow extraction of the activation energy, assuming Arrhenius behaviour (Extended Data Fig. 2a). Extrapolation using the activation energy allows estimation of ^{7}Li diffusion at room temperature and facilitates comparison to other materials (Table 1, Extended Data Table 1).

GITT diffusion coefficient and diffusion length. Information on electrode thermodynamics, including phase transitions, and lithium kinetics[74] can in principle be extracted from GITT measurements by tracking the voltage evolution after a brief current pulse as lithium diffuses and the chemical potential equilibrates within the electrode/particles. Reliable quantitative diffusion coefficients, D_{Li}, are however difficult to extract from GITT alone. To determine a diffusion coefficient from GITT measurements, a diffusion length (L) must be defined. However, a battery electrode is a heterogeneous system. First, it is a composite of active material (here, metal oxide), porous carbon and polymeric binder. Within this composite, there is a distribution of particle sizes (unless single crystals[75] or well defined particles are used; even then, diffusion varies with lattice direction). Furthermore, different regimes of diffusion must exist because of the presence of solid/liquid interfaces and porous electrode structure. Nevertheless, in an electrode that does not undergo severe pulverization (for example, an intercalation electrode), L is a fixed quantity throughout the experiment. Variation in L—a parameter required to relate the rate of relaxation to the diffusion—causes values of D_{Li} to vary considerably between reports, even for the same material[28,76]. Thus, although a physically meaningful diffusion coefficient may not be extracted, a relative measure of diffusion is readily obtained. For this reason, we use an extracted proxy for lithium diffusion ($D_{Li}L^{-2}$; Extended Data Fig. 1), which removes the uncertainty in L and enables self-consistent analysis of a single electrode and electrodes prepared under identical conditions. The addition of quantitative information from another method (for example, NMR spectroscopy or tracer diffusion) allows us to calibrate relative changes in Li^+ kinetics to quantitative diffusion values throughout a range of lithiation.

$Nb_{18}W_{16}O_{93}$ operando diffraction mechanism. As shown in Fig. 4d, lithiation from 0 to 0.2 Li^+/TM is characterized by a–b-plane expansion. The plateau-like region from 0.2 to 0.3 Li^+/TM is associated with further a–b-plane expansion, still maintaining the $b \approx 3a$ superstructure and contraction of the layers (c axis). From 0.3 to 0.55 Li^+/TM, the structure expands nearly isotropically, whereas at about 0.55 Li^+/TM, the pseudo-superstructure relationship collapses. From this point until 0.75 Li^+/TM, b contracts rapidly, a expands and c is constant. At 0.75 Li^+/TM, the layers begin to expand back to their initial interlayer spacing while b continues contracting, albeit at a slower rate, to its initial length, and a continues its expansion. Thus, when fully lithiated to 1.0 Li^+/TM ($Li_{34}Nb_{18}W_{16}O_{93}$), b and c are within ±0.1% of the unlithiated host, while a, and thus the total volume expansion, is +2.8%. In the multi-redox region beyond 1.0 Li^+/TM, the structure again expands somewhat isotropically.

Structure family extensions. Regarding the electronic structure changes of $Nb_{16}W_5O_{55}$ and $Nb_{18}W_{16}O_{93}$ upon lithiation, related partially reduced phases may be considered. Very high electronic conductivities are known to exist in the crystallographic shear niobium tungsten oxides[77], as well as related partially reduced versions of both families, for example, shear $Nb_{12}O_{29}$[78] and bronze $A_{0.3}WO_3$[79] (A = alkali metal cation), which exhibit resistivities lower than 10^{-2} Ω cm.

For ionic diffusion, there are also analogies between the new lithiated complex oxides and superionic conductors, such as α-AgI[80] and $Li_{10}GeP_2S_{12}$[81,82], in that there are multiple sites for the cations to occupy within a disordered three-dimensional structure[83,84].

In the composition and phase space of block and bronze structures, cation (such as early transition metals, p-block elements, aliovalent mixed metals)[27,75,77,85,86] and anion (such as oxyfluorides[27,87,88]) dopants make it possible to tune the ionic and electronic properties and thereby affect voltage, capacity, power capability and stability. Analogues are known with Na^+, K^+, Mg^{2+} and Ca^{2+}, which suggests that the variety of possible tunnel shapes and sizes, vacant sites and three-dimensional connectivities is also promising for beyond-Li electrochemical energy storage, according to the insights into high rate and capacity discovered here.

Application considerations. Fast charging or high-power delivery from a full cell requires a cathode to match the anode. Although $LiFePO_4$ has been used as a promising high-rate cathode[89], along with $Li_4Ti_5O_{12}$, both of these electrodes have exceptionally flat voltage profiles. The $LiFePO_4$–$Li_4Ti_5O_{12}$ cathode–anode combination provides a constant voltage but presents a serious challenge in terms of battery management systems (BMS). Simple and accurate BMS are crucial for battery applications in electric vehicles and mobile technology and are even more important at high rates for preventing dangerous and degradative over(dis)charging while maximizing utility. BMS rely on their ability to measure the state of charge, which cannot be done by charge counting alone as the battery degrades. The open-circuit voltage is a more reliable measure and a thermodynamic quantity. In contrast to the $Li_4Ti_5O_{12}$/$LiFePO_4$ battery, the sloping voltage profiles of the new high-rate materials presented herein provide an opportunity for the modelling and electrochemical engineering/industrial communities to develop BMS based on sloping voltage profiles, which may prove to be a substantial commercial advantage for $Nb_{16}W_5O_{55}$, $Nb_{18}W_{16}O_{93}$ and related materials in the growing area of high-power/fast-charging applications.

High-voltage anode materials, such as the niobium tungsten oxides, have several further advantages. Above 1.0 V versus Li^+/Li^0, the formation of solid–electrolyte interphase is minimal, which means that Li will not be lost into side reactions with the electrolyte. Furthermore, in a full cell against, for example, $LiFePO_4$, $LiN(CF_3SO_2)_2$ can be used to replace the more toxic $LiPF_6$ electrolyte salt without degrading Al current collector(s)[89], and Al can be used as the current collector instead of the more expensive Cu while avoiding LiAl alloying potentials (≤0.3 V versus Li^+/Li)[90]. Another incentive to find replacements for nano-$Li_4Ti_5O_{12}$ is the issue of gas evolution and associated swelling or pressure build-up[91,92], which stems from heterogeneous catalysis between the metal-oxide surface and the organic electrolyte. The small particle sizes required to compensate for poor Li^+ and electronic diffusion in $Li_4Ti_5O_{12}$ increase the reactive surface area, and the much smaller surface area of the ~5-μm $Nb_{16}W_5O_{55}$ or $Nb_{18}W_{16}O_{93}$ particles potentially reduces side reactions.

Data availability. The data that support the findings of this study are available from www.repository.cam.ac.uk and the corresponding author upon reasonable request.

55. Roth, R. S. Thermal stability of long range order in oxides. *Prog. Solid State Chem.* **13**, 159–192 (1980).
56. Eyring L. & O'Keefe M. (eds) *The Chemistry of Extended Defects in Non-Metallic Solids* (North-Holland, Amsterdam, 1970).
57. Toby, B. H. & Von Dreele, R. B. GSAS-II: the genesis of a modern open-source all purpose crystallography software package. *J. Appl. Cryst.* **46**, 544–549 (2013).
58. Allpress, J. G. & Roth, R. S. The effect of annealing on the concentration of Wadsley defects in the Nb_2O_5—WO_3 system. *J. Solid State Chem.* **3**, 209–216 (1971).
59. Ragone, D. V. Review of battery systems for electrically powered vehicles. In Proc. Mid-Year Meeting of the Society of Automotive Engineers (SAE, 1968).
60. Rohatgi, A. *WebPlotDigitizer* https://automeris.io/WebPlotDigitizer (2017).
61. Borkiewicz, O. J. et al. The AMPIX electrochemical cell: a versatile apparatus for *in situ* X-ray scattering and spectroscopic measurements. *J. Appl. Cryst.* **45**, 1261–1269 (2012).
62. Caglioti, G., Paoletti, A., Ricci, F. P. Choice of collimators for a crystal spectrometer for neutron diffraction. *Nucl. Instrum.* **3**, 223–228 (1958).
63. Ravel, B. & Newville, M. ATHENA, ARTEMIS, HEPHAESTUS: data analysis for X-ray absorption spectroscopy using IFEFFIT. *J. Synchrotron Radiat.* **12**, 537–541 (2005).

64. Newville, M. IFEFFIT: interactive XAFS analysis and FEFF fitting. *J. Synchrotron Radiat.* **8**, 322–324 (2001).
65. Thompson, A. et al. *X-ray Data Booklet* (Lawrence Berkeley National Laboratory, Berkeley, 2009).
66. Yamamoto, T., Orita, A. & Tanaka, T. Structural analysis of tungsten–zirconium oxide catalyst by W K-edge and L_1-edge XAFS. *X-ray Spectrom.* **37**, 226–231 (2008).
67. Tougerti, A. et al. XANES study of rhenium oxide compounds at the L_1 and L_3 absorption edges. *Phys. Rev. B* **85**, 125136 (2012).
68. Jayarathne, U. et al. X-ray absorption spectroscopy systematics at the tungsten L-edge. *Inorg. Chem.* **53**, 8230–8241 (2014).
69. Drube, W., Treusch, R., Sham, T. K., Bzowski, A. & Soldatov, A. V. Sublifetime-resolution Ag L_3-edge XANES studies of Ag-Au alloys. *Phys. Rev. B* **58**, 6871–6876 (1998).
70. Bersuker, I. B. *The Jahn–Teller Effect* (Cambridge Univ. Press, Cambridge, 2006).
71. Whittle, T. A., Schmid, S. & Howard, C. J. Octahedral tilting in the tungsten bronzes. *Acta Crystallogr. B* **71**, 342–348 (2015).
72. Yan, L. et al. Electrospun $WNb_{12}O_{33}$ nanowires: superior lithium storage capability and their working mechanism. *J. Mater. Chem. A* **5**, 8972–8980 (2017).
73. Stejskal, E. O. & Tanner, J. E. Spin diffusion measurements: spin echoes in the presence of a time-dependent field gradient. *J. Chem. Phys.* **42**, 288–292 (1965).
74. Weppner, W. & Huggins, R. A. Determination of the kinetic parameters of mixed-conducting electrodes and application to the system Li_3Sb. *J. Electrochem. Soc.* **124**, 1569–1578 (1977).
75. Shu, G. J. & Chou, F. C. Sodium-ion diffusion and ordering in single-crystal P2-Na_xCoO_2. *Phys. Rev. B* **78**, 052101 (2008).
76. Reddy, M. V. et al. Studies on the lithium ion diffusion coefficients of electrospun Nb_2O_5 nanostructures using galvanostatic intermittent titration and electrochemical impedance spectroscopy. *Electrochim. Acta* **128**, 198–202 (2014).
77. Ruscher, C., Salje, E. & Hussain, A. The effect of the Nb-W distribution on polaronic transport in ternary Nb-W oxides: electrical and optical properties. *J. Phys. C* **21**, 4465–4480 (1988).
78. Cava, R. J. et al. Electrical and magnetic properties of $Nb_2O_{5-\delta}$ crystallographic shear structures. *Phys. Rev. B* **44**, 6973–6981 (1991).
79. Dickens, P. G. & Whittingham, M. S. The tungsten bronzes and related compounds. *Q. Rev. Chem. Soc.* **22**, 30–44 (1968).
80. Hull, S. Superionics: crystal structures and conduction processes. *Rep. Prog. Phys.* **67**, 1233–1314 (2004).
81. Kamaya, N. et al. A lithium superionic conductor. *Nat. Mater.* **10**, 682–686 (2011).
82. Kuhn, A., Duppel, V. & Lotsch, B. V. Tetragonal $Li_{10}GeP_2S_{12}$ and Li_7GePS_8 – exploring the Li ion dynamics in LGPS Li electrolytes. *Energy Environ. Sci.* **6**, 3548–3552 (2013).
83. Mo, Y., Ong, S. P. & Ceder, G. First principles study of the $Li_{10}GeP_2S_{12}$ lithium super ionic conductor material. *Chem. Mater.* **24**, 15–17 (2012).
84. Phani Dathar, G. K., Balachandran, J., Kent, P. R. C., Rondinone, A. J. & Ganesh, P. Li-ion site disorder driven superionic conductivity in solid electrolytes: a first-principles investigation of β-Li_3PS_4. *J. Mater. Chem. A* **5**, 1153–1159 (2017).
85. Bevan, D. J. M. & Hagenmuller, D. *Non-Stoichiometric Compounds: Tungsten Bronzes, Vanadium Bronzes and Related Compounds 1st edn* (Pergamon Press, Exeter, 1973).
86. Pinus, I., Catti, M., Ruffo, R., Salamone, M. M. & Mari, C. M. Neutron diffraction and electrochemical study of $FeNb_{11}O_{29}$/$Li_{11}FeNb_{11}O_{29}$ for lithium battery anode applications. *Chem. Mater.* **26**, 2203–2209 (2014).
87. Galy, J. & Andersson, S. Structure cristalline de $MoNb_{15}O_{40}F$. *Acta Crystallogr. B* **24**, 1027–1031 (1968).
88. Idrees, F. et al. Facile synthesis of novel Nb_3O_7F nanoflowers, their optical and photocatalytic properties. *CrystEngComm* **15**, 8146–8152 (2013).
89. Zaghib, K., Mauger, A., Groult, H., Goodenough, J. B. & Julien, C. M. Advanced electrodes for high power Li-ion batteries. *Materials* **6**, 1028–1049 (2013).
90. Wen, C. J., Boukamp, B. A., Huggins, R. A. & Weppner, W. Thermodynamic and mass transport properties of "LiAl". *J. Electrochem. Soc.* **126**, 2258–2266 (1979).
91. He, Y.-B. et al. Gassing in $Li_4Ti_5O_{12}$-based batteries and its remedy. *Sci. Rep.* **2**, 913 (2012).
92. Lv, W., Gu, J., Niu, Y., Wen, K. & He, W. Review—gassing mechanism and suppressing solutions in $Li_4Ti_5O_{12}$-based lithium-ion batteries. *J. Electrochem. Soc.* **164**, A2213–A2224 (2017).
93. Vinod Chandran, C. & Heitjans, P. Solid-state NMR studies of lithium ion dynamics across materials classes. *Ann. Rep. NMR Spectrosc.* **89**, 1–102 (2016).
94. Wang, Z. et al. Lithium diffusion in lithium nitride by pulsed-field gradient NMR. *Phys. Chem. Chem. Phys.* **14**, 13535–13538 (2012).
95. Kuhn, A. et al. A new ultrafast superionic Li-conductor: ion dynamics in $Li_{11}Si_2PS_{12}$ and comparison with other tetragonal LGPS-type electrolytes. *Phys. Chem. Chem. Phys.* **16**, 14669–14674 (2014).
96. Kaus, M. et al. Local structures and Li ion dynamics in a $Li_{10}SnP_2S_{12}$-based composite observed by multinuclear solid-state NMR spectroscopy. *J. Phys. Chem. C* **121**, 23370–23376 (2017).
97. Hayamizu, K. & Aihara, Y. Lithium ion diffusion in solid electrolyte $(Li_2S)_7(P_2S_5)_3$ measured by pulsed-gradient spin-echo ^{7}Li NMR spectroscopy. *Solid State Ion.* **238**, 7–14 (2013).
98. Gobet, M., Greenbaum, S., Sahu, G. & Liang, C. Structural evolution and Li dynamics in nanophase Li_3PS_4 by solid-state and pulsed-field gradient NMR. *Chem. Mater.* **26**, 3558–3564 (2014).
99. Hayamizu, K. et al. NMR studies on lithium ion migration in sulfide-based conductors, amorphous and crystalline Li_3PS_4. *Solid State Ion.* **285**, 51–58 (2016).
100. Holzmann, T. et al. $Li_{0.6}[Li_{0.2}Sn_{0.8}S_2]$ – a layered lithium superionic conductor. *Energy Environ. Sci.* **9**, 2578–2585 (2016).
101. Ishiyama, H. et al. Nanoscale diffusion tracing by radioactive ^{8}Li tracer. *Jpn. J. Appl. Phys.* **53**, 110303 (2014).
102. Holz, M. & Weingartner, H. Calibration in accurate spin-echo self-diffusion measurements using ^{1}H and less-common nuclei. *J. Magn. Reson.* **92**, 115–125 (1991).
103. Hayamizu, K. Temperature dependence of self-diffusion coefficients of ions and solvents in ethylene carbonate, propylene carbonate, and diethyl carbonate single solutions and ethylene carbonate + diethyl carbonate binary solutions of $LiPF_6$ studied by NMR. *J. Chem. Eng. Data* **57**, 2012–2017 (2012).
104. Chowdhury, M. T., Takekawa, R., Iwai, Y., Kuwata, N. & Kawamura, J. Lithium ion diffusion in Li β-alumina single crystals measured by pulsed field gradient NMR spectroscopy. *J. Chem. Phys.* **140**, 124509 (2014).
105. Hayamizu, K. & Seki, S. Long-range Li ion diffusion in NASICON-type $Li_{1.5}Al_{0.5}Ge_{1.5}(PO_4)_3$ (LAGP) studied by ^{7}Li pulsed-gradient spin-echo NMR. *Phys. Chem. Chem. Phys.* **19**, 23483–23491 (2017).
106. Arbi, K. et al. Ionic mobility in Nasicon-type $LiM^{IV}2(PO_4)_3$ materials followed by ^{7}Li NMR spectroscopy. *MRS Proc.* **1313** (2011).
107. Hayamizu, K., Matsuda, Y., Matsui, M. & Imanishi, N. Lithium ion diffusion measurements on a garnet-type solid conductor $Li_{6.6}La_3Zr_{1.6}Ta_{0.4}O_{12}$ by using a pulsed-gradient spin-echo NMR method. *Solid State Nucl. Magn. Reson.* **70**, 21–27 (2015).
108. Kuhn, A. et al. Li self-diffusion in garnet-type $Li_7La_3Zr_2O_{12}$ as probed directly by diffusion-induced ^{7}Li spin-lattice relaxation NMR spectroscopy. *Phys. Rev. B* **83**, 094302 (2011).
109. Langer, J., Epp, V., Heitjans, P., Mautner, F. A. & Wilkening, M. Lithium motion in the anode material LiC_6 as seen via time-domain ^{7}Li NMR. *Phys. Rev. B* **88**, 094304 (2013).
110. Mali, M., Roos, J., Sonderegger, M., Brinkmann, D. & Heitjans, P. ^{6}Li and ^{7}Li diffusion coefficients in solid lithium measured by the NMR pulsed field gradient technique. *J. Phys. F Met. Phys.* **18**, 403–412 (1988).
111. Sugiyama, J. et al. Li-ion diffusion in $Li_4Ti_5O_{12}$ and $LiTi_2O_4$ battery materials detected by muon spin spectroscopy. *Phys. Rev. B* **92**, 014417 (2015).
112. Sugiyama, J. et al. Lithium diffusion in spinel $Li_4Ti_5O_{12}$ and $LiTi_2O_4$ films detected with ^{8}Li beta-NMR. *Phys. Rev. B* **96**, 094402 (2017).
113. Wilkening, M. et al. Microscopic Li self-diffusion parameters in the lithiated anode material $Li_{4+x}Ti_5O_{12}$ ($0 \leq x \leq 3$) measured by ^{7}Li solid state NMR. *Phys. Chem. Chem. Phys.* **9**, 6199–6202 (2007).
114. Ruprecht, B., Wilkening, M., Uecker, R. & Heitjans, P. Extremely slow Li ion dynamics in monoclinic Li_2TiO_3—probing macroscopic jump diffusion via ^{7}Li NMR stimulated echoes. *Phys. Chem. Chem. Phys.* **14**, 11974–11980 (2012).
115. Wagemaker, M., van de Krol, R., Kentgens, A. P. M., van Well, A. A. & Mulder, F. M. Two phase morphology limits lithium diffusion in TiO_2 (anatase): a ^{7}Li MAS NMR study. *J. Am. Chem. Soc.* **123**, 11454–11461 (2001).
116. Wagemaker, M. et al. The influence of size on phase morphology and Li-ion mobility in nanosized lithiated anatase TiO_2. *Chem. Eur. J.* **13**, 2023–2028 (2007).
117. Verhoeven, V. W. J. et al. Lithium dynamics in $LiMn_2O_4$ probed directly by two-dimensional ^{7}Li NMR. *Phys. Rev. Lett.* **86**, 4314–4317 (2001).
118. Ishiyama, H. et al. Direct measurement of nanoscale lithium diffusion in solid battery materials using radioactive tracer of ^{8}Li. *Nucl. Instrum. Methods B* **376**, 379–381 (2016).
119. Bork, D. & Heitjans, P. NMR relaxation study of ion dynamics in nanocrystalline and polycrystalline $LiNbO_3$. *J. Phys. Chem. B* **102**, 7303–7306 (1998).
120. Ruprecht, B. & Heitjans, P. Ultraslow lithium diffusion in Li_3NbO_4 probed by ^{7}Li stimulated echo NMR spectroscopy. *Diffusion Fundamentals* **12**, 100–101 (2010).
121. Sale, M. & Avdeev, M. 3DBVSMAPPER: a program for automatically generating bond-valence sum landscapes. *J. Appl. Crystallogr.* **45**, 1054–1056 (2012).
122. Avdeev, M., Sale, M., Adams, S. & Rao, R. P. Screening of the alkali-metal ion containing materials from the Inorganic Crystal Structure Database (ICSD) for high ionic conductivity pathways using the bond valence method. *Solid State Ion.* **225**, 43–46 (2012).
123. Brown, I. D. *The Chemical Bond in Inorganic Chemistry: The Bond Valence Model* (Oxford Univ. Press, Oxford, 2002).

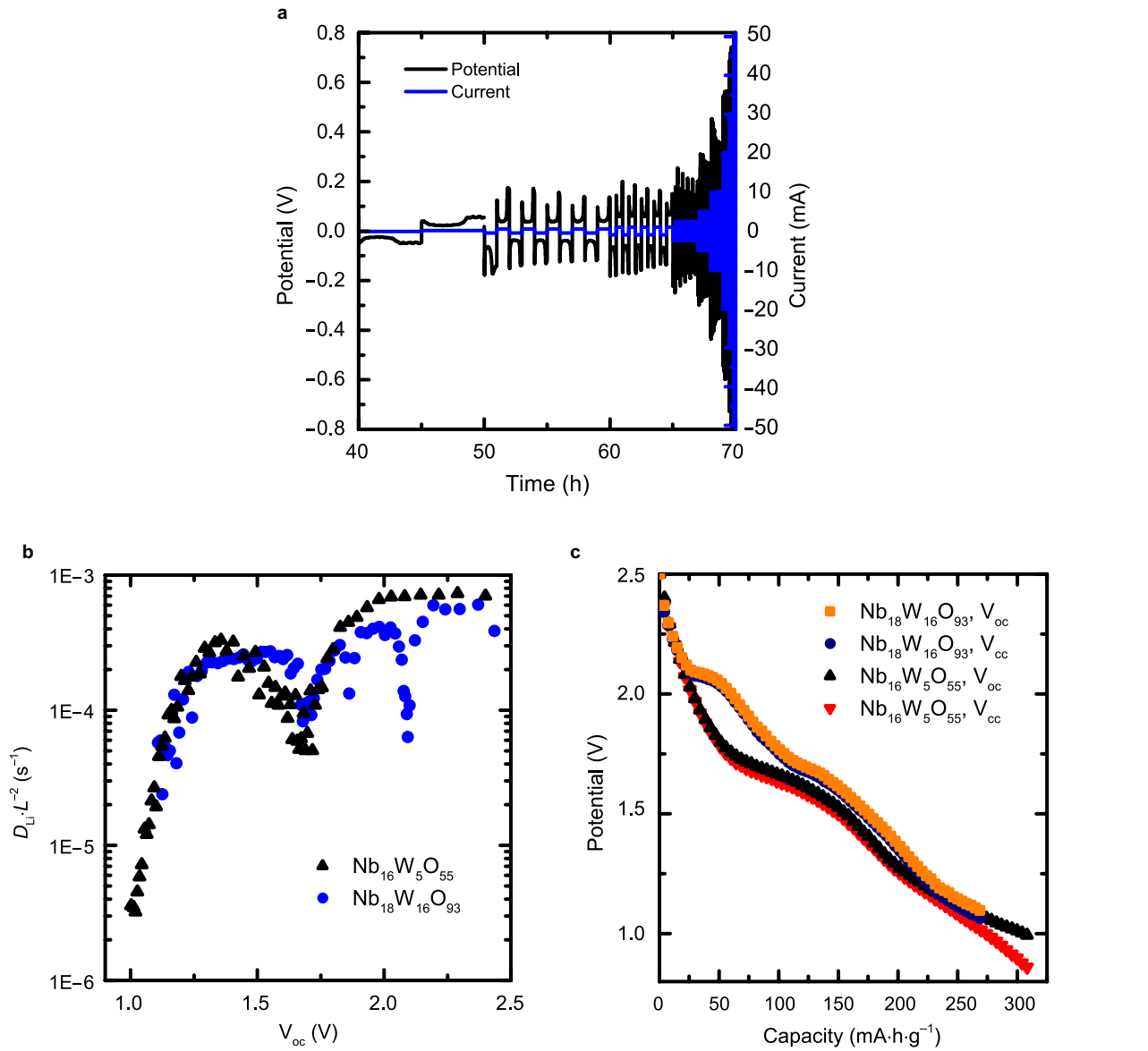

Extended Data Fig. 1 | Overpotential in Li||Li symmetric cells and GITT of niobium tungsten oxides. a, Li||Li symmetric cells were configured identically to those used for metal-oxide testing, with the exception of a second Li disk replacing the composite electrode. Rate testing was carried out with current densities corresponding to the rates shown in Fig. 2a–e, with 5 cycles at 100 μA (C/5), 500 μA (1C), 1 mA (2C), 2.5 mA (5C) and 5 mA (10C) and 10 cycles at 10 mA (20C), 20 mA (40C), 30 mA (60C) and 50 mA (100C). The 'rates' in parentheses indicate the inverse of the time (in hours) that the current was applied, simulating the conditions (current densities, periods of applied current and thus total charge transferred) of the rate test experiments. An excerpt of the results is shown here from the fifth cycle at C/5 until the end of the test; the test was performed twice with the same overpotentials observed in both cells. At low current densities, below 1 mA (2C), the overpotential is below 100 mV; however, at 5 mA (10C) the overpotential rises to 200 mV and increases to about 700 mV at 100C. **b**, **c**, Relative changes in lithium diffusion as a function of open-circuit voltage (V_{oc}; **b**) and open-circuit voltage versus closed-circuit voltage (V_{cc}; **c**) from the GITT measurements. The plot in **c** shows the 'thermodynamic' electrochemical profiles at C/20 with a 12-h rest period at each point, reaching a full discharge in approximately one month. In $Nb_{16}W_5O_{55}$, the fastest diffusion is observed from the dilute limit to $Li_{4.5(5)}Nb_{16}W_5O_{55}$, dropping by two orders of magnitude in the low-voltage window, where more than 1 Li^+/TM are incorporated. The GITT data indicate that the second electrochemical region of $Nb_{16}W_5O_{55}$ is broader than typically observed in a two-phase reaction, but the observed discontinuity in the $D_{Li}L^{-2}$ values in this region suggests that $Nb_{16}W_5O_{55}$ approaches two-phase behaviour. The average diffusion coefficient in $Nb_{18}W_{16}O_{93}$ is similar to that of $Nb_{16}W_5O_{55}$. The bronze also displays discontinuities in $D_{Li}L^{-2}$ at 2.1, 1.85 and 1.7 V. In both phases, the low-voltage region (below 1.25 V, well over 1 Li^+/TM) is characterized by an increasing overpotential and suppressed kinetics.

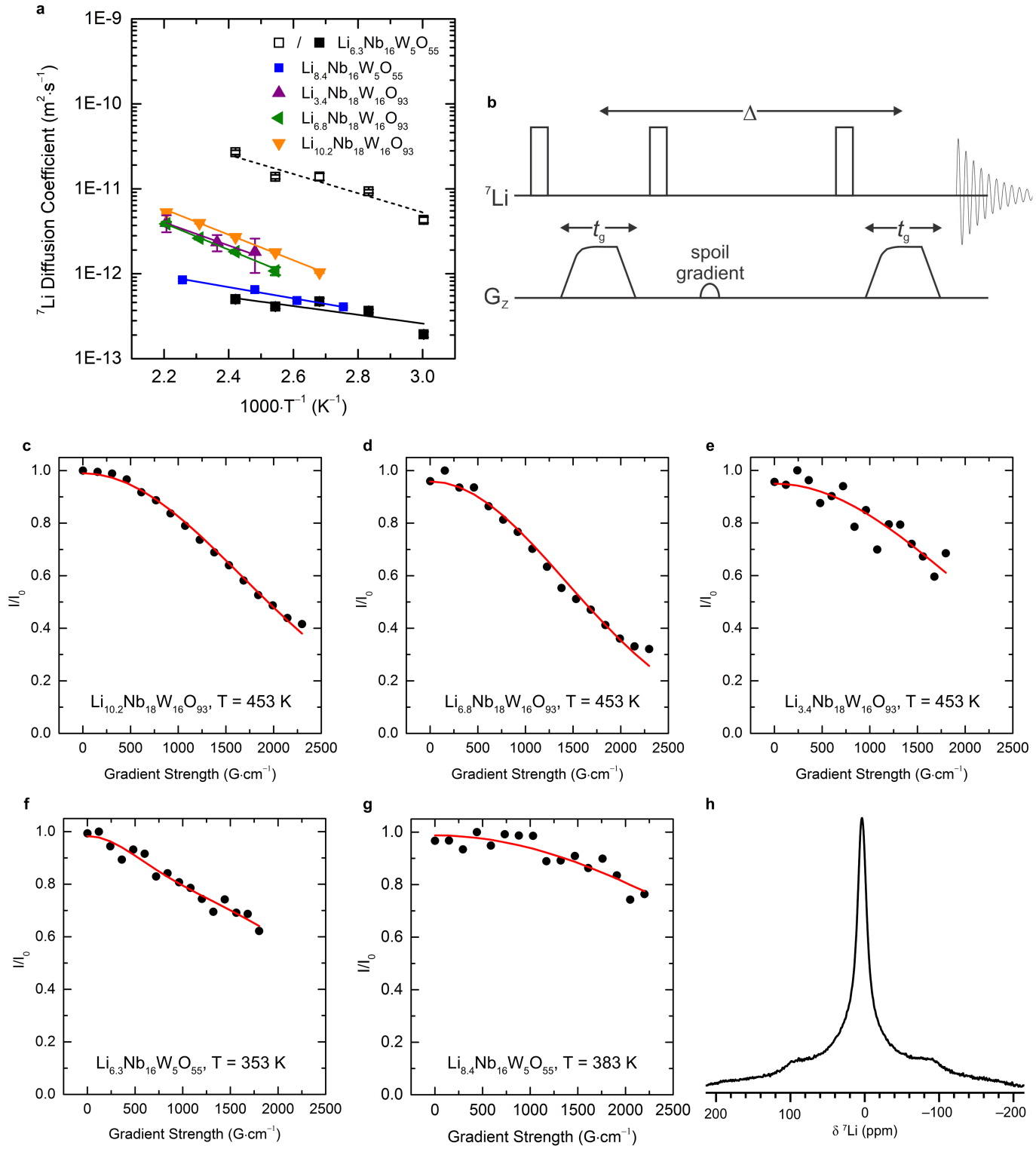

Extended Data Fig. 2 | See next page for caption.

Extended Data Fig. 2 | Lithium diffusion from ^{7}Li PFG NMR spectroscopy. a, The lithium diffusion coefficients of $Li_xNb_{16}W_5O_{55}$ ($x = 6.3$, 8.4) and $Li_xNb_{18}W_{16}O_{93}$ ($x = 3.4$, 6.8, 10.2) were measured in the temperature range 333–453 K (Table 1). The filled (85% signal contribution) and empty (15% signal contribution) symbols for $Li_{6.3}Nb_{16}W_5O_{55}$ correspond to the observed two-component diffusion (see main text and Methods). In most cases, the error bars (2σ, obtained from the fit) are smaller than the sizes of the points. **b**, Stimulated-echo PFG sequence used to measure ^{7}Li diffusivities, showing both radiofrequency (^{7}Li) and magnetic-field-gradient (G_z) pulses. Here, the gradient pulse duration (t_g) includes the up-ramping, time on and down-ramping of the opt composite gradient pulses. During Δ, a short spoiler gradient was used to remove residual transverse magnetization. **c–g**, Representative ^{7}Li decay curves showing the normalized NMR signal intensity as a function of gradient strength for the bronze structures $Li_{10.2}Nb_{18}W_{16}O_{93}$ at 453 K (**c**), $Li_{6.8}Nb_{18}W_{16}O_{93}$ at 453 K (**d**) and $Li_{3.4}Nb_{18}W_{16}O_{93}$ at 453 K (**e**) and the block structures $Li_{6.3}Nb_{16}W_5O_{55}$ at 353 K (**f**) and $Li_{8.4}Nb_{16}W_5O_{55}$ at 383 K (**g**). Black circles represent experimental data points and red lines represent mono- (**c–e**, **g**) or biexponential (**f**) fits to the data by the Stejskal–Tanner equation. Biexponential fits to all samples except $Li_{6.3}Nb_{16}W_5O_{55}$ did not lead to improved fits over those obtained with monoexponential fits. The poor signal-to-noise ratio of $Li_{6.3}Nb_{16}W_5O_{55}$, even with more than 100 mg of electrode sample, did not allow us to explore alternative models beyond the mono- and biexponential models, such as models considering the effect of anisotropic diffusion, which manifests as subtle differences in echo attenuation[94]. **h**, A representative one-dimensional ^{7}Li NMR spectrum ($Li_{8.4}Nb_{16}W_5O_{55}$, static, 403 K) showing the shift (δ ^{7}Li) region and lineshape.

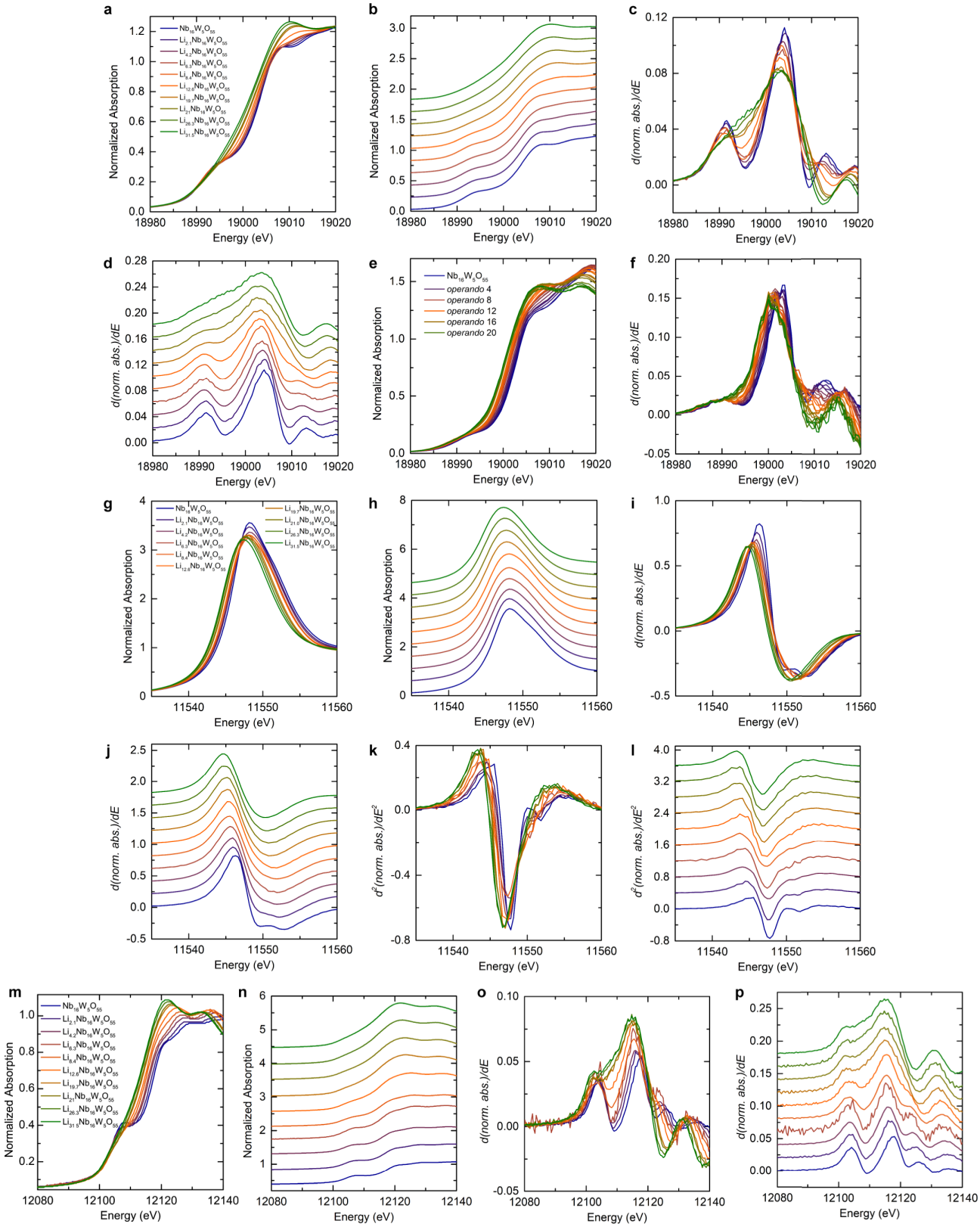

Extended Data Fig. 3 | $Nb_{16}W_5O_{55}$ X-ray absorption spectroscopy. **a**–**d**, $Li_xNb_{16}W_5O_{55}$ ex situ (see Supplementary Fig. 14) Nb K edge XANES spectra (**a**, **b**) and derivative spectra (**c**, **d**). **e**, **f**, Operando Nb K edge XANES spectra of $Nb_{16}W_5O_{55}$ and 22 discharge spectra, with each successive spectrum at about +11 mA h g^{-1} (**e**), and operando derivative spectra (**f**; 23 spectra shown, 5 colours labelled). The pre-edge and main edge are at about 18,991 and 19,004 eV, respectively. Spectra in **b** and **d** are vertically offset by 0.2 and 0.02, respectively, for clarity. **g**–**l**, $Li_xNb_{16}W_5O_{55}$ ex situ W L_{II} edge XANES spectra (**g**, **h**), derivative spectra (**i**, **j**) and second-derivative spectra (**k**, **l**). Spectra in **h**, **j** and **l** are vertically offset by 0.5, 0.2 and 0.4, respectively, for clarity. **m**–**p**, $Li_xNb_{16}W_5O_{55}$ ex situ W L_I edge XANES spectra (**m**, **n**) and derivative spectra (**o**, **p**) near the W L_I absorption edge. The pre-edge is at about 12,104 eV and the main edge at about 12,117 eV. Spectra are vertically offset by 0.5 in **n** and by 0.02 in **p** for clarity.

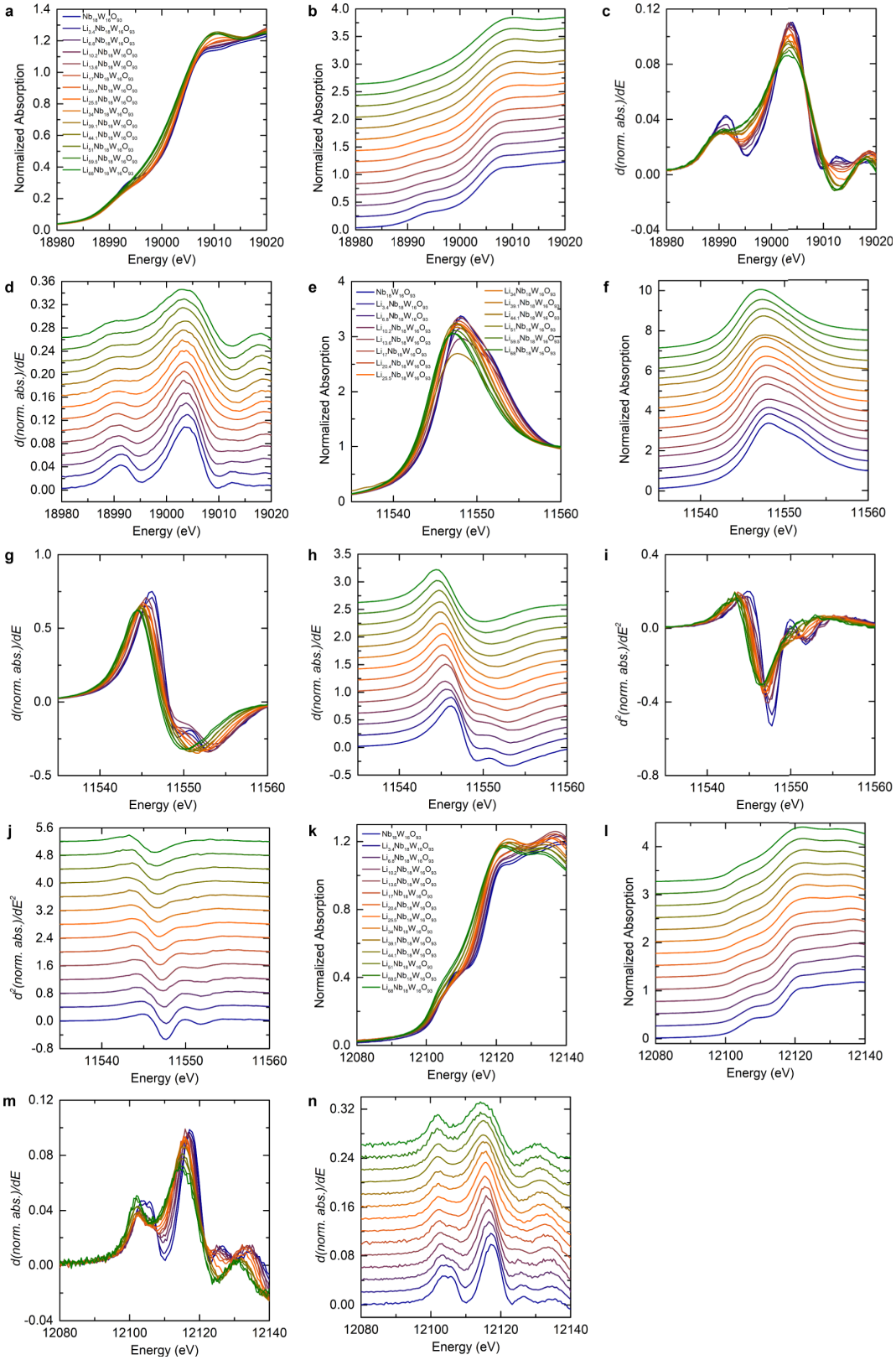

Extended Data Fig. 4 | $Nb_{18}W_{16}O_{93}$ X-ray absorption spectroscopy. **a–d**, $Li_xNb_{18}W_{16}O_{93}$ ex situ Nb K edge XANES spectra (**a**, **b**) and derivative spectra (**c**, **d**). The pre-edge and main edge are at about 18,991 and 19,004 eV, respectively. Spectra in **b** and **d** are vertically offset by 0.2 and 0.02, respectively, for clarity. **e–j**, $Li_xNb_{18}W_{16}O_{93}$ ex situ W L_{II} edge XANES spectra (**e**, **f**), derivative spectra (**g**, **h**) and second-derivative spectra (**i**, **j**). Spectra in **f**, **h** and **j** are vertically offset by 0.5, 0.2 and 0.4, respectively, for clarity. **k–m**, $Li_xNb_{18}W_{16}O_{93}$ ex situ W L_I edge XANES spectra (**k**, **l**) and derivative spectra (**m**, **n**) near the W L_I absorption edge. The pre-edge is at about 12,104 eV and the main edge at about 12,117 eV. Spectra are vertically offset by 0.25 in **l** and by 0.02 in **n** for clarity.

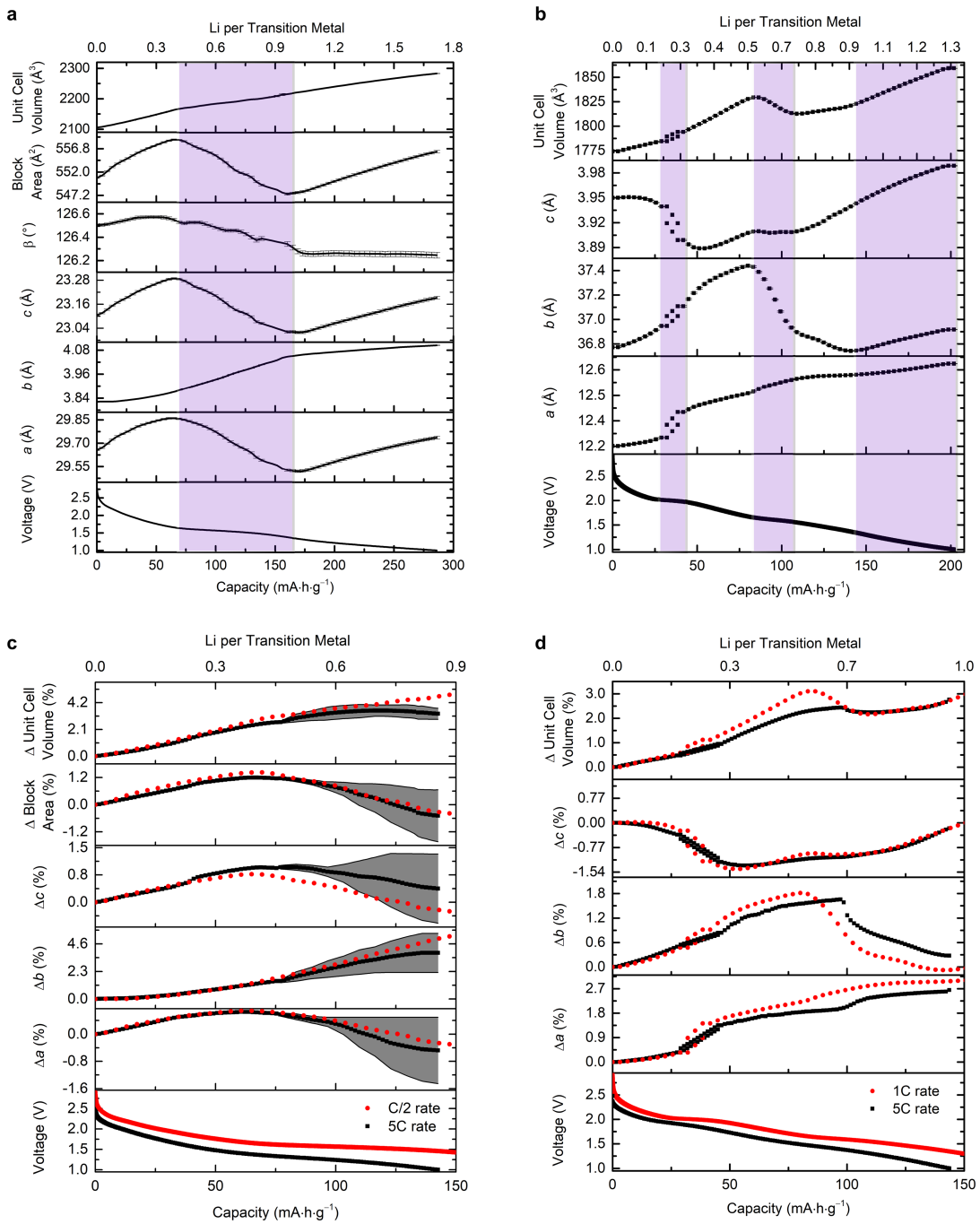

Extended Data Fig. 5 | Lattice evolution of $Nb_{16}W_5O_{55}$ and $Nb_{18}W_{16}O_{93}$ upon lithiation. a, **b**, Absolute lattice parameter values resulting from Rietveld refinement of operando diffraction data, analogous to that of Fig. 4c, $Nb_{16}W_5O_{55}$ (**a**) and Fig. 4d, $Nb_{18}W_{16}O_{93}$ (**b**). Error bars show the standard deviation of each parameter, as estimated from the fits (approximately equal to the symbol height in **b**). Shading distinguishes the different structural regions. For $Nb_{18}W_{16}O_{93}$, the second stage (two-phase region) contains two sets of lattice parameters. **c**, Structure evolution of $Nb_{16}W_5O_{55}$ as a function of rate. At high rates, the lithiation reaction becomes inhomogeneous (Extended Data Fig. 6) and cannot be fitted with a single set of lattice parameters over the whole electrode. The shaded grey area for the 5C data corresponds to the range of each unit-cell parameter. **d**, Structure evolution of $Nb_{18}W_{16}O_{93}$ as a function of rate. The mechanism of $Li_xNb_{18}W_{16}O_{93}$ lattice evolution does not appear to be strongly rate-dependent. The reaction extends further at lower rates within the same voltage range, partly because of a smaller overpotential at lower current densities (Extended Data Fig. 1a).

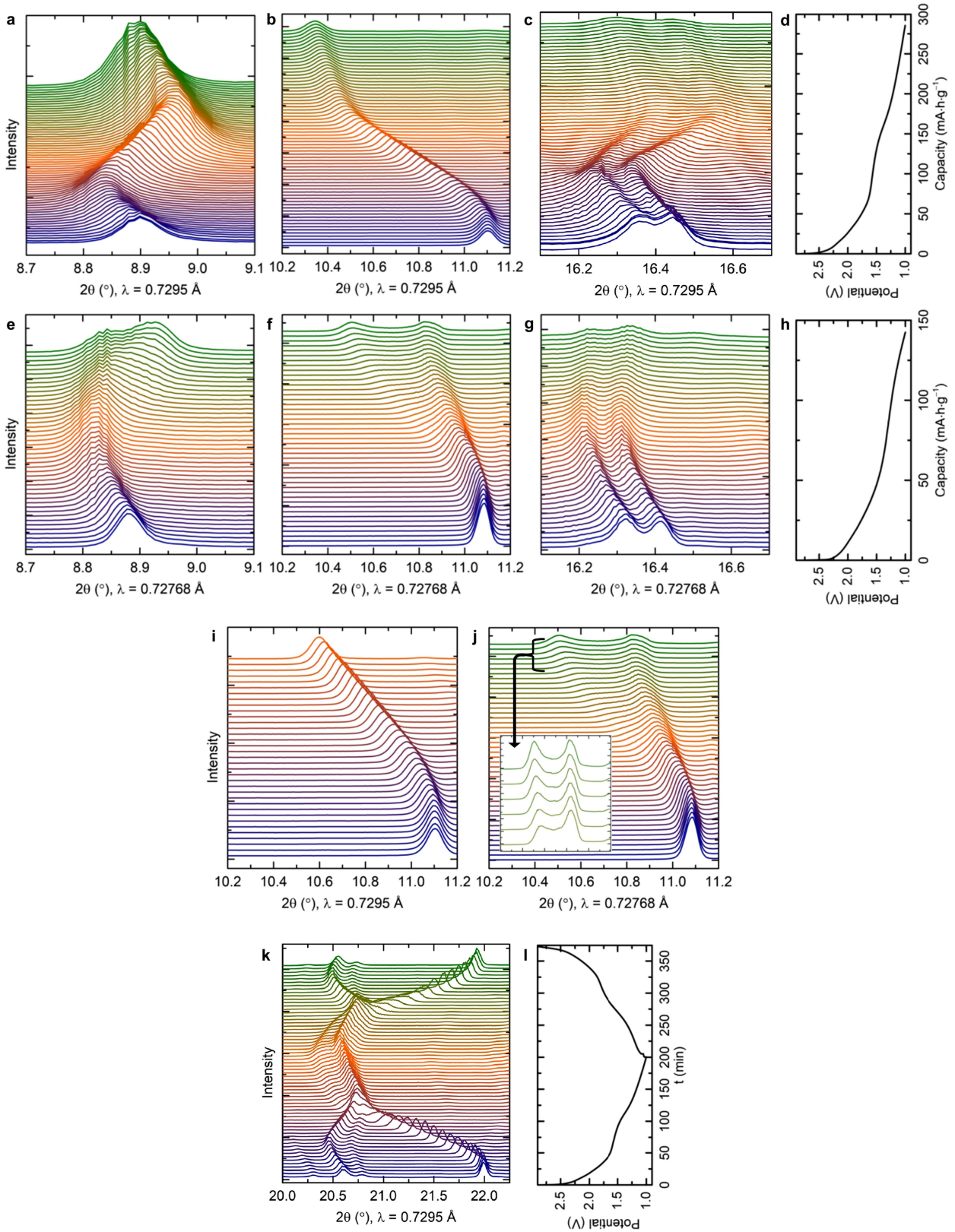

Extended Data Fig. 6 | See next page for caption.

Extended Data Fig. 6 | Solid-solution structure evolution and reversibility of $Nb_{16}W_5O_{55}$. **a**–**c**, Profile evolution of selected reflections at C/2 and **d**, the corresponding electrochemical discharge profile. **e**–**g**, Profile evolution of selected reflections at 5C and **h**, the corresponding electrochemical discharge profile. **a**, **e**, $(60\overline{4})$. **b**, **f**, overlapping (110) and $(11\bar{1})$. **c**, **g**, $(10\ 0\bar{1})$ (left) and $(60\overline{9})$ (right), with smaller overlapping reflections. The evolution in each case commences analogously; as lithiation increases, the structure evolution at high rate becomes inhomogeneous and the contraction of the *ac* block is not fully realized. **i**, The overlapping (110) and $(11\bar{1})$ reflections shift smoothly to larger *d* spacing (smaller 2θ) for the entire sample at C/2, whereas in **j**, there is substantial intensity across a range of 2θ values at high rate. This inter-peak intensity is shown more clearly in the inset of **j**. The intensity range represents a range of lattice parameters (Extended Data Fig. 5c) and an inhomogeneous solid-solution reaction probably resulting from inhomogeneous lithium transport and concentration gradients within the electrolyte[33,34]. Diffraction patterns are shown from 0 to about 145 mA h g^{-1} (ascending), which corresponds to the full 5C discharge and partial C/2 discharge. **k**, **l**, Structure reversibility over a full electrochemical lithiation/delithiation cycle of $Nb_{16}W_5O_{55}$ at C/2. In **k**, the $(14\ 0\overline{9})$/(407) (left) and (020) (right) reflections are displayed over a full operando synchrotron X-ray diffraction discharge–charge cycle from 3.0 to 1.0 V with multi-redox (de)lithiation. The symmetry of discharge and charge is apparent, although a small amount of lithium remains in the structure after charging (Extended Data Fig. 7).

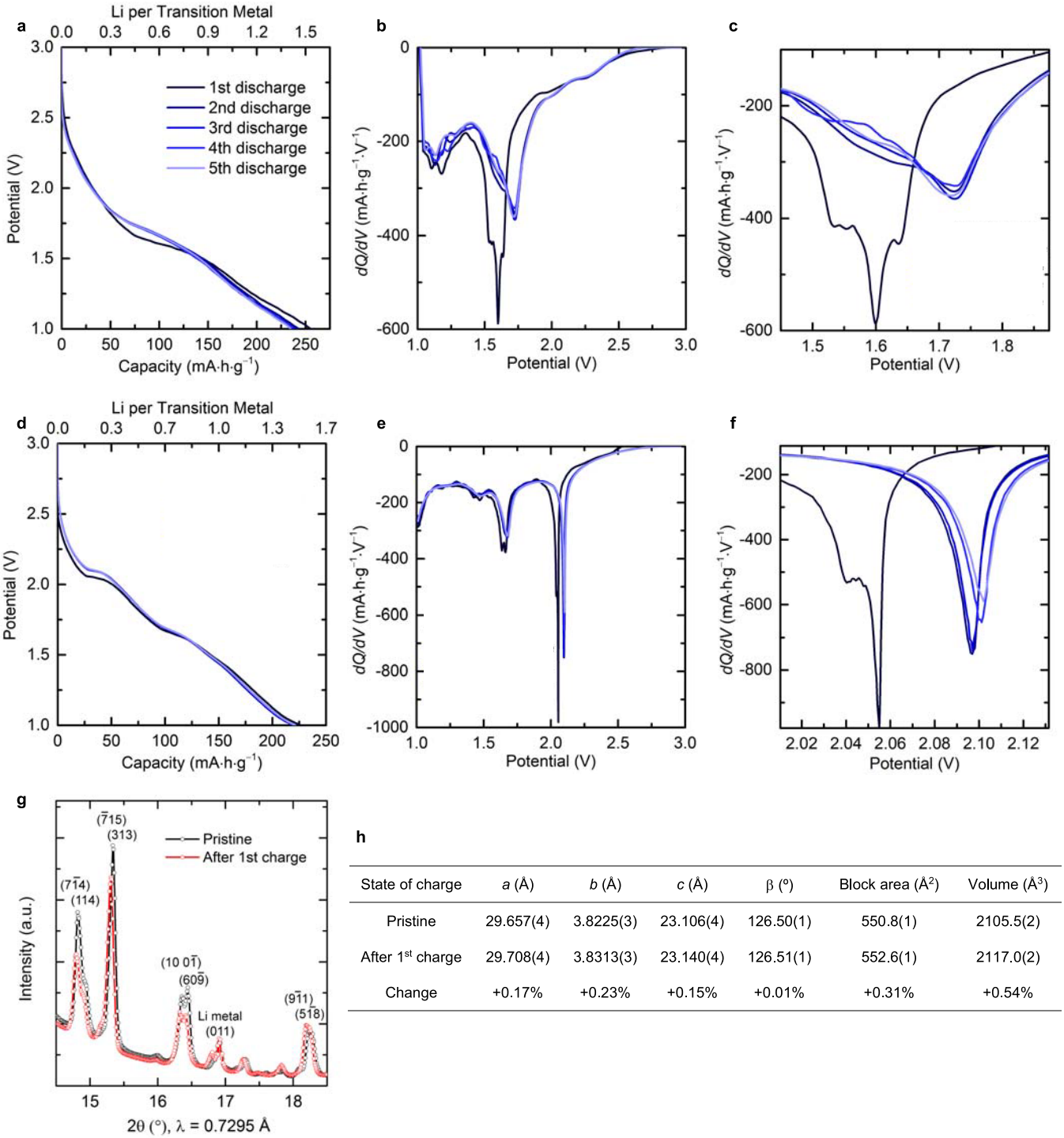

h

State of charge	*a* (Å)	*b* (Å)	*c* (Å)	β (°)	Block area (Å^2)	Volume (Å^3)
Pristine	29.657(4)	3.8225(3)	23.106(4)	126.50(1)	550.8(1)	2105.5(2)
After 1st charge	29.708(4)	3.8313(3)	23.140(4)	126.51(1)	552.6(1)	2117.0(2)
Change	+0.17%	+0.23%	+0.15%	+0.01%	+0.31%	+0.54%

Extended Data Fig. 7 | Electrochemical profile evolution and early-cycle lithium retention of $Nb_{16}W_5O_{55}$ and $Nb_{18}W_{16}O_{93}$. a–f, There is an activation process on the first cycle for $Nb_{16}W_5O_{55}$ (**a–c**) and $Nb_{18}W_{16}O_{93}$ (**d–f**), which extends to a much smaller extent in the next several cycles, leading to an increase in intercalation voltage at the first 'plateau-like' feature and a broadening of the d*Q*/d*V* peaks (**b**, **c**, **e, f**). The phenomenon is associated with a retention of lithium in the structure. The occurrence of this activation phenomenon is structure-independent, indicating that it may have an electronic origin. The electrochemical data in **a–f** were collected at C/5 but the phenomenon is also observed at other rates. **g**, Diffraction patterns of $Nb_{16}W_5O_{55}$ before lithiation and after the first charge from operando measurements at C/2. **h**, Lattice parameters of the pristine and charged structure show changes that indicate that some lithium was retained in the structure after charging the electrode, commensurate with the changes from first- to second-cycle electrochemistry.

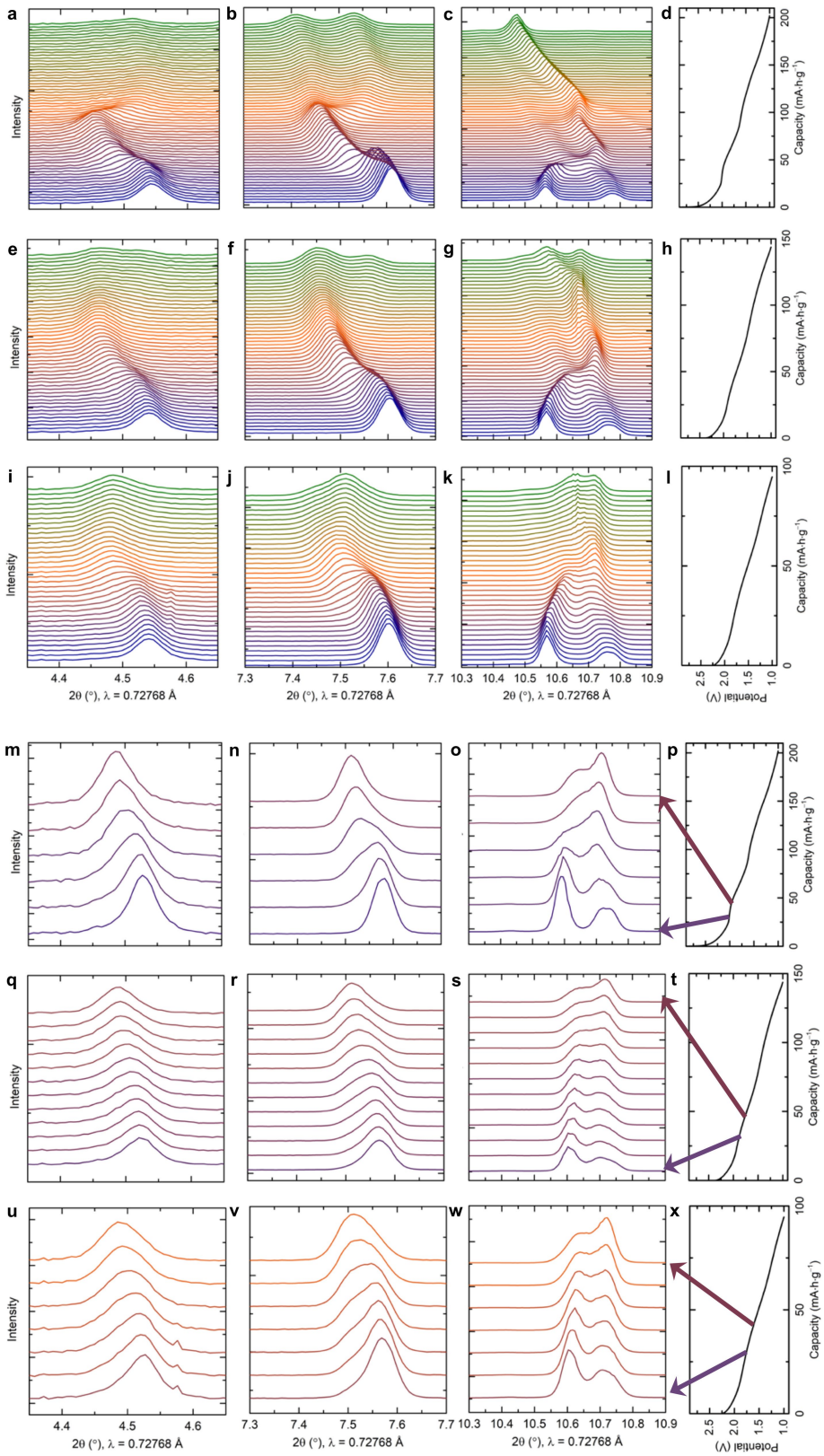

Extended Data Fig. 8 | Operando X-ray diffraction patterns of $Nb_{18}W_{16}O_{93}$ from 1C to 10C. a–l, The profile evolution of selected reflections and the corresponding electrochemical discharge profile is shown at 1C (**a**–**d**), 5C (**e**–**h**) and 10C (**i**–**l**). **a**, **e**, **i**, (040); **b**, **f**, **j**, overlapped (230) and (160); **c**, **g**, **k**, (001) (left, initially) and overlapped (330) and (190) (right, initially). The evolution in each case is similar in mechanism and differs in the extent of reaction, consistent with the electrochemical profiles. **m**–**x**, The two-phase region of $Li_xNb_{18}W_{16}O_{93}$ for $x \approx 6.6$–10.2 as a function of rate. Selected regions of the diffraction pattern at shown at 1C (**m**–**p**), 5C (**q**–**t**) and 10C (**u**–**x**). **m**, **q**, **u**, (040); **n**, **r**, **v**, overlapped (230) and (160); **o**, **s**, **w**, (001) (left, initially) and overlapped (330) and (190) (right, initially). The arrows from the electrochemical discharge profiles in **p**, **t** and **x** correspond to the first and last diffraction patterns collected in the two-phase region (about 29–45 mA h g^{-1}), as indicated. Metastable intermediates that can occur at high rates in two-phase systems such as $LiFePO_4$ would be difficult to distinguish in this system owing to the small compositional and structural changes that are associated with the $Li_{6.6}Nb_{18}W_{16}O_{93}$ to $Li_{10.2}Nb_{18}W_{16}O_{93}$ two-phase reaction.

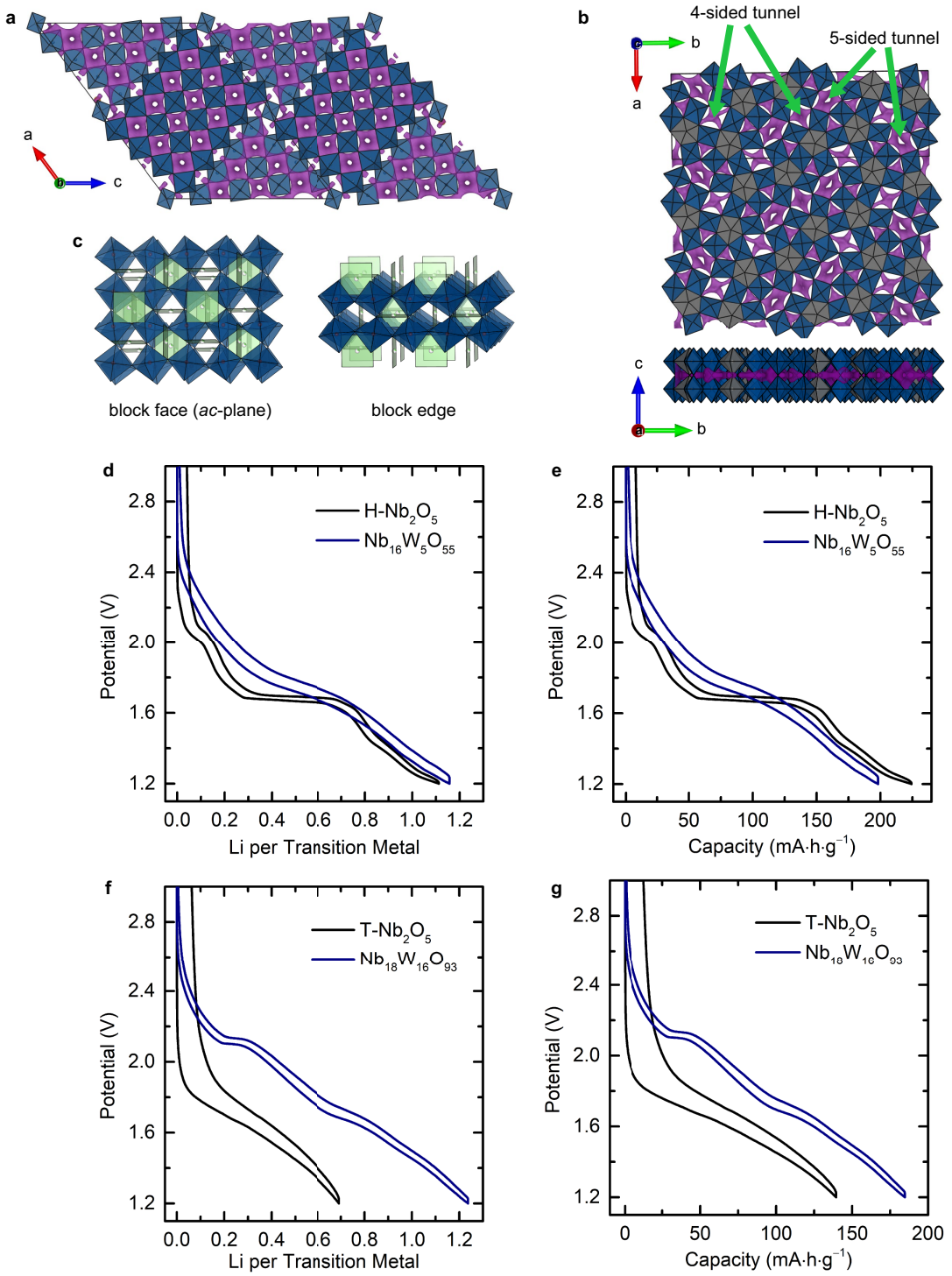

Extended Data Fig. 9 | Prospective lithium positions and pathways in block-type and bronze-type ternary niobium tungsten oxides and electrochemical comparisons to binary niobium oxides. a, **b**, Bond valence sum maps of $Nb_{16}W_5O_{55}$ (**a**) and $Nb_{18}W_{16}O_{93}$ (**b**) depict stable lithium positions and pathways according to bond valence energy landscape calculations performed in 3DBVSMAPPER[121]. Calculations were performed over a fine grid with $149 \times 20 \times 116$ points computed for $Nb_{16}W_5O_{55}$ and $61 \times 184 \times 20$ points computed for $Nb_{18}W_{16}O_{93}$ along their respective crystallographic axes. Isosurface levels are shown at '2.0 eV', which is a parameter used to visualize ionic pathways and not a quantitative estimation. The bond valence sum and bond valence energy landscape provide an indication of lithium positions and diffusion pathways in complex or novel systems and have shown good agreement with experimental and computational investigations of structure and dynamics[121–123]. **c**, Possible intrablock lithium positions for $Nb_{16}W_5O_{55}$ based on Li_xMO_3 in the low-lithium regime, before it undergoes intercalant-induced distortion. **d**, **e**, Block phases $Nb_{16}W_5O_{55}$ and H-Nb_2O_5 are compared on the basis of Li^+/TM (**d**) and gravimetric capacity (**e**) on the third cycle at C/5. **f**, **g**, Bronze-like phases $Nb_{18}W_{16}O_{93}$ and T-Nb_2O_5 are compared on the basis of Li^+/TM (**f**) and gravimetric capacity (**g**) on the third cycle at C/5.

Extended Data Table 1 | Lithium self-diffusion coefficients of lithium-ion battery electrode materials, solid electrolytes, liquid electrolytes and reference compounds

Compound	Structure Type	D_{Li} ($m^2 \cdot s^{-1}$)	T (K)	Technique	Reference
$Li_{6.3}Nb_{16}W_5O_{55}$	Block, *cs*	2.1×10^{-12} / 1.7×10^{-13}	298	PFG NMR (extrapolated)	This work
$Li_{6.3}Nb_{16}W_5O_{55}$	Block, *cs*	2.7×10^{-11} / 5.2×10^{-13}	413	PFG NMR	This work
$Li_{8.4}Nb_{16}W_5O_{55}$	Block, *cs*	1.6×10^{-13}	298	PFG NMR (extrapolated)	This work
$Li_{8.4}Nb_{16}W_5O_{55}$	Block, *cs*	6.5×10^{-13}	403	PFG NMR	This work
$Li_{3.4}Nb_{18}W_{16}O_{93}$	Bronze-like	1.1×10^{-13}	298	PFG NMR (extrapolated)	This work
$Li_{3.4}Nb_{18}W_{16}O_{93}$	Bronze-like	2.0×10^{-12}	413	PFG NMR	This work
$Li_{6.8}Nb_{18}W_{16}O_{93}$	Bronze-like	1.1×10^{-13}	298	PFG NMR (extrapolated)	This work
$Li_{6.8}Nb_{18}W_{16}O_{93}$	Bronze-like	1.8×10^{-12}	413	PFG NMR	This work
$Li_{10.2}Nb_{18}W_{16}O_{93}$	Bronze-like	1.1×10^{-13}	298	PFG NMR (extrapolated)	This work
$Li_{10.2}Nb_{18}W_{16}O_{93}$	Bronze-like	2.7×10^{-12}	413	PFG NMR	This work
$Li_{10}GeP_2S_{12}$	Thio-LISICON	2×10^{-12}	298	PFG NMR	[82]
$Li_{10}GeP_2S_{12}$	Thio-LISICON	4×10^{-11}	453	PFG NMR	[82]
Li_7GePS_8	Thio-LISICON	2×10^{-12}	298	PFG NMR	[82]
Li_7GePS_8	Thio-LISICON	4×10^{-11}	453	PFG NMR	[82]
$Li_{10}SnP_2S_{12}$	Thio-LISICON	1.4×10^{-12}	298	PFG NMR	[95,96]
$Li_{10}SnP_2S_{12}$	Thio-LISICON	4×10^{-11}	453	PFG NMR	[95]
$Li_{11}Si_2PS_{12}$	Thio-LISICON	3.5×10^{-12}	298	PFG NMR	[95]
$Li_{11}Si_2PS_{12}$	Thio-LISICON	4×10^{-11}	453	PFG NMR	[95]
$Li_7P_3S_{11}$	Thio-LISICON	$1–5\times10^{-12}$	303	PFG NMR	[97]
$Li_7P_3S_{11}$	Thio-LISICON	$2–11\times10^{-12}$	353	PFG NMR	[97]
β-Li_3PS_4	Thio-LISICON	5.4×10^{-13}	373	PFG NMR	[98]
amorphous-Li_3PS_4	Amorphous (Thio-LISICON)	6.5×10^{-13}	303	PFG NMR	[99]
amorphous-Li_3PS_4	Amorphous (Thio-LISICON)	$1.6–3.4\times10^{-12}$	353	PFG NMR	[99]
$Li_{0.6}[Li_{0.2}Sn_{0.8}S_2]$	Layered (O1)	$2–20\times10^{-12}$	298	PFG NMR	[100]
$Li_{0.6}[Li_{0.2}Sn_{0.8}S_2]$	Layered (O1)	2.6×10^{-10}	407	PFG NMR	[100]
$Li_{3.4}V_{0.6}Si_{0.4}O_4$	LISICON	5×10^{-15}	333	tracer	[101]
0.25 M LiCl (aq.)	Solution	9.6×10^{-10}	298	PFG NMR	[102]
1.0 M $LiPF_6$ in PC	Liquid electrolyte	8.3×10^{-11}	298	PFG NMR	[103]
1.0 M $LiPF_6$ in EC	Liquid electrolyte	9.9×10^{-11}	298	PFG NMR	[103]
1.0 M $LiPF_6$ in DEC	Liquid electrolyte	2.5×10^{-10}	298	PFG NMR	[103]
Li β-alumina (*ab* plane)	β-alumina	1.2×10^{-11}	298	PFG NMR	[104]
Li β-alumina (*c*-axis)	β-alumina	6.4×10^{-13}	333	PFG NMR	[104]
Li_3N	Li_3N	1.4×10^{-10}	534	PFG NMR	[94]
$Li_{1.5}Al_{0.5}Ge_{1.5}(PO_4)_3$	NASICON	2.9×10^{-13}	311	PFG NMR	[105]
$Li_{1.2}Al_{0.2}Ti_{1.8}(PO_4)_3$	NASICON	1.5×10^{-12}	250	NMR relaxometry + PFG NMR	[106]
$Li_{6.6}La_3Zr_{1.6}Ta_{0.4}O_{12}$	Garnet	3.5×10^{-13}	353	PFG NMR	[107]
$Li_7La_3Zr_2O_{12}$	Garnet	1.8×10^{-18}	298	NMR relaxometry	[108]
$Li_7La_3Zr_2O_{12}$	Garnet	1.3×10^{-17}	325	NMR relaxometry	[108]
$Li_7La_3Zr_2O_{12}$	Garnet	3.3×10^{-14}	530	NMR relaxometry	[108]
Graphite (Stage I)	Graphite	$1–2\times10^{-15}$	298	NMR relaxometry	[109]
Li metal	bcc	5×10^{-15}	298	PFG NMR (extrapolated)	[110]
Li metal	bcc	1×10^{-12}	400	PFG NMR	[110]
$Li_4Ti_5O_{12}$	Spinel	3.2×10^{-15}	298	μ^+-SR	[111,112]
$Li_{5.7}Ti_5O_{12}$	Spinel	2.7×10^{-16}	298	NMR relaxometry	[113]
$LiTi_2O_4$	Spinel	3.6×10^{-15}	298	μ^+-SR	[111]
β-Li_2TiO_3	Li_2SnO_3	2×10^{-17}	433	NMR relaxometry	[114]
Li_xTiO_2 (x = 0.12) micro	Anatase component	4.7×10^{-16}	293	NMR relaxometry	[115]
Li_xTiO_2 (x = 0.12) micro	Li-titanate component	1.3×10^{-15}	293	NMR relaxometry	[115]
Li_xTiO_2 (x = 0.06) nano	Anatase component	1.9×10^{-16}	293	NMR relaxometry	[116]
Li_xTiO_2 (x = 0.06) nano	Li-titanate component	5.7×10^{-16}	293	NMR relaxometry	[116]
Li_xTiO_2 (x = 0.12) nano	Anatase component	1.1×10^{-16}	293	NMR relaxometry	[116]
Li_xTiO_2 (x = 0.12) nano	Li-titanate component	1.8×10^{-16}	293	NMR relaxometry	[116]
Li_xTiO_2 (x = 0.12) nano	Li-titanate component	4.9×10^{-16}	413	NMR relaxometry	[116]
$Li_{0.55}TiO_2$ nano	Li-titanate	1.7×10^{-16}	293	NMR relaxometry	[116]
$Li_{0.55}TiO_2$ nano	Li-titanate	4.6×10^{-16}	413	NMR relaxometry	[116]
$LiFePO_4$	Olivine	$1–6\times10^{-20}$	300	DFT/Tracer	[49,50]
$LiMn_2O_4$	Spinel	1×10^{-20}	350	NMR relaxometry	[117]
$LiMn_2O_4$	Spinel	1.8×10^{-16}	623	Tracer	[118]
$LiNbO_3$	$LiNbO_3$	7.5×10^{-15}	890	NMR relaxometry	[119]
Li_3NbO_4	Li_3NbO_4	4×10^{-21}	353	NMR relaxometry	[120]
Li_3NbO_4	Li_3NbO_4	1×10^{-16}	553	NMR relaxometry	[120]

Battery electrode materials are not typically amenable to the direct measurement of lithium diffusion via PFG NMR owing to rapid paramagnetic (T_1 and T_2) relaxation and slow diffusion. The weak paramagnetism (as indicated by the small NMR shift) and ultrafast diffusion of block-phase $Nb_{16}W_5O_{55}$ and bronze-like-phase $Nb_{18}W_{16}O_{93}$ enabled PFG NMR measurement, but only at slightly elevated temperature, where the T_2 relaxation time was increased. Room-temperature D_{Li} values were calculated by extrapolating from the elevated temperature data and assuming Arrhenius behaviour. Lithium diffusion measurements from NMR relaxometry are included here for several anode materials in which diffusion is too slow to be measured by PFG NMR[93]. cs, crystallographic shear; LISICON, lithium superionic conductor; NASICON, sodium superionic conductor; O1, layered structure with octahedral lithium and single-layer repeat stacking of transition-metal layers; PC, propylene carbonate; bcc, body-centred cubic; μ^+-SR, muon spin resonance; DFT, density functional theory.